Master Thesis

Prototype Design for a Lunar Lander High Resolution Stereo Camera

Author:
Shreya Champakbhai Chauhan
Matriculation Nr: 5574616

Supervisors:
Prof. Dr. Ralf Jaumann
Dr. Doris Breuer

Research Facility:
German Aerospace Center (DLR), Berlin
Planetary Sensor Systems, Institute of Space Research
Advisors: Dr. Matthias Grott, Christian Althaus

A thesis submitted in fulfilment of the requirements for the degree of M.Sc. Planetary Sciences and Space Exploration

in the

Planetary Sciences and Remote Sensing
Institute of Geological Sciences

Freie Universität Berlin

June 17, 2025

Declaration of Authorship

I, Shreya Champakbhai Chauhan, declare that this thesis titled, "Prototype Design for a Lunar Lander High Resolution Stereo Camera" and the work presented in it are my own. I confirm that I have written this thesis independently and have not used any resources other than those indicated.

Signed: _____

Date: _____

Declaration of the Use of AI-tools

I hereby declare that in the drafting, and revision of the work attached, I have made use of generative AI tools in the following ways:

- To assist with revising passages for concision and editing for spelling and grammar
- To improve the language of my own phrases, sentences, paragraphs and revise transitional phrasing
- To generate and/or troubleshooting programming code

I have use the AI-tools in an ethical manner, and verified it for any false contents before including in my work. I have indicated the use of AI-tool in a transparent way, similar to any other sources, wherever it was utilised.

Signed: _____

Date: _____

Abstract

Traditional stereo cameras used in terrestrial exploration, particularly on rovers, typically rely on binocular optical designs that are large, bulky, and often include moving parts. This thesis presents a design concept for a breadboard prototype which is developed and built using commercial off-the-shelf (COTS) components. This allows for rapid prototyping, cost-effective testing, and performance evaluation under simulated mission conditions. By utilizing a single-detector stereo vision, the system can effectively create 3D reconstructions of observed object with a spatial resolution of $54\,\mu$m/px,and depth resolution of $<1\,$mm/px, enabling precise depth mapping. The optical performance and its scientific applications were validated with experiments such as the resolution test, shape measurement, static angle of repose and relative albedo measurements. The stereo camera developed in this project demonstrates capabilities for high-resolution, in-situ lunar surface analysis based on regolith characterization. Overall, the camera's design balances compactness with performance, overcoming challenges related to baseline constraints, environmental exposure, and computational efficiency faced by conventional stereo cameras. This imaging system offers a valuable tool for future lunar lander and rover missions, supporting in-depth scientific investigations.

Keywords: lunar exploration, rover instrumentation, stereo vision, 3D reconstruction, monocular stereo camera, photogrammetry, regolith characterisation

Acknowledgements

I am thankful to the former director of the Institute of Space Research, Prof. Dr. Heike Rauer, and the head of the Department of Planetary Sensor Systems, Dr. Matthias Grott, for giving me the opportunity to work at the German Aerospace Center (DLR) in Berlin-Adlershof. I thank Prof. Dr. Ralf Jaumann and Dr. Doris Breuer for agreeing to be the supervisor and examiner of this thesis work and for providing their valuable feedback whenever needed. I am deeply grateful to Christian Althaus for being my primary advisor throughout my work and for always taking the time to support me whenever I faced challenges. I am also grateful to the members of the Planetary Sensor Systems (PSS) working group at DLR for sharing their experiences and providing me with recommendations.

A special thanks to Jan Binger for assisting me in the laboratory and to Frank Trauthan for sharing his expertise in stereo cameras.

I would like to extend my sincere thanks to Dr. Solmaz Adeli and Dr. Jörn Helbert from the Department of Planetary Laboratories at DLR, who first gave me the opportunity to be a project intern in their group and introduced me to the PSS group to continue working at DLR for my master's thesis. It has been a great learning experience, and I was able to immerse myself in an esteemed research environment at DLR, which has greatly strengthened my confidence in my professional skills as a planetary scientist.

Finally, I'd like to thank my family, whose support made reaching this stage of education possible. My fellow colleagues at DLR and Freie Universität, Berlin, who helped and supported me in this academic journey. I am also grateful to my friends and classmates for proof reading, their editing help, feedback sessions, and moral support. I could not have undertaken this journey without my partner Sabrina Rücker, who always believed in me and reminded me to take breaks. Their belief in me has kept my spirits and motivation high during this process.

Contents

List of Figures

List of Tables

List of Symbols

H_s	sensor size	mm
P_c	pixel count	-
P_s	pixel size	mm
θ	cant angle	$^\circ$
H_t	height above ground	mm
W_{d_1}	working distance for nearest object in focus	mm
W_{d_2}	working distance for farthest object in focus	mm
f	focal length	mm
$f\#$	f number	-
FOV	field of view	mm
$AFOV$	angular field of view	$^\circ$
$iFOV$	instantaneous field of view	μrad
ξ_{image}	image space resolution	lp/mm
ξ_{object}	object space resolution	lp/mm
δ_z	depth resolution	$mm/pixel$
m	system magnification	-
B	stereo baseline length	mm
DOF_o	depth of focus	mm
CoC	circle of confusion	mm
ϕ_A	aperture diameter	mm
H_f	hyper-focal distance	mm
D_n	nearest distance of acceptable sharpness	mm
D_f	farthest distance of acceptable sharpness	mm
DOF_c	depth of field	mm
c_x, c_y	position of optical centre	$pixels$
f_x, f_y	focal length	$pixels$
s	skew coefficient	-
α_t	tilt angle of the left and right mirrors	$^\circ$
Z	depth	mm
$I(x, y)$	pixel intensity	-
$\rho(x, y)$	relative surface albedo	-
L_x, L_y, L_z	light direction vector	mm
$N_(x, y)$	surface normal vector	mm

Dedicated to my parents...

Chapter 1

Introduction

1.1 Background

Lunar exploration has been crucial to better understand the formation of Earth and our Solar System. The lunar surface and its composition provides evidence of historical geological events since its formation. Hence, investigating it has been a target of space exploration. Humanities first step towards space exploration started with lunar missions like NASA's Apollo program, allowing the development of state-of-the-art technologies for in-situ resource utilization. These legacies are continued with future missions such as NASA's Artemis program. Interacting and navigating with the lunar surface and acquiring scientific data were some of the challenges highlighted during these missions. The lunar lander plays a critical role in enabling in-situ exploration of the Moon. One significant challenge it must address is the presence of fine dust particles in the top layer of the lunar surface, known as regolith. These particles pose serious risks to mission safety, rover mobility, and the optimal functioning of scientific instruments [2, 3].

1.2 Existing Camera Systems on Lunar Missions

Stereo imaging systems designed to support autonomous navigation, terrain analysis, and scientific application, have been successfully utilised in various space missions, involving lander and robotic rovers operation [4]. The general principle of such an imaging system is on the basis of binocular stereo vision, acquiring images with slightly different viewpoints. The system can then reconstruct a three dimensional representation of the terrain, allowing accurate depth estimation and spatial context of the surrounding.

For example, the Chinese Chang'e-3 and Chang'e-4 lunar rovers are equipped with stereo cameras for terrain mapping and obstacle detection [5, 6]. These systems have enabled the rovers to navigate the lunar surface with a high degree of autonomy, even in low-visibility conditions [7, 8].

Across these missions, the common theme is the use of binocular stereo vision as a core technique for 3D perception. The two-camera configuration allows for the triangulation of depth information, which is critical for safe and efficient rover operation. In particular, stereo vision is extensively used for:

- Navigation and path planning: By generating 3D terrain models, stereo cameras enable rovers to identify safe and feasible paths.
- Hazard detection: Stereo imaging helps in identifying obstacles such as rocks, slopes, and craters that could impede the rover's movement.

- Context imaging: Stereo cameras provide a broader, more immersive view of the planetary surface, supporting scientific analysis and mission planning.
- Detection of in-situ science target: Stereo imaging assists in identifying and selecting geological features for closer examination.

In addition to lunar missions, stereo vision have also been employed in Mars exploration. One of the most notable examples is the Mars Exploration Rovers (MER), Spirit and Opportunity, which were launched in 2003 and operated on the Martian surface for several years. Each rover was equipped with a pair of navigation cameras (Navcams) mounted on a mast, providing stereo imagery for terrain mapping and hazard detection. These cameras were essential for path planning and obstacle avoidance, allowing the rovers to traverse complex and uneven terrain autonomously [3, 9].

The Mars Science Laboratory (MSL) rover Curiosity, launched in 2011, further advanced the use of stereo vision in planetary exploration. Curiosity features a stereo pair of Navigation Cameras (Navcams) and a stereo pair of Mast Cameras (Mastcam), which provide high-resolution stereo imagery for both navigation and scientific analysis. The Mastcam is capable of capturing colour stereo images, enabling the creation of detailed 3D models of the Martian surface and supporting geological investigations [3, 10].

More recently, the Perseverance rover, part of the Mars 2020 mission, includes an enhanced stereo imaging system with multiple camera pairs, including the Navigation Cameras (Navcams), the Mastcam-Z system, and the SuperCam remote imaging system [3, 11]. The Mastcam-Z, in particular, is a zoom-able stereo camera system that allows for high-resolution, colour, and 3D imaging over a wide range of distances. This system not only supports navigation and hazard detection, but also provides valuable context for scientific investigations, such as the study of rock formations and potential signs of past life in the Jezero crater [12].

While binocular cameras remains the dominant approach, recent advancements in computational imaging and sensor technology are opening the door to alternative methods for stereo vision, such as monocular depth estimation and multi-camera systems. However, the reliability, simplicity, and well-established performance of binocular stereo vision continue to make it the preferred choice for planetary rovers.

Parameter	**Mars 2020** MastCam-Z [12]	**Mars 2020** Navcam [11]	**ExoMars** PanCam WAC [13]	**ExoMars** PanCam HRC [13]	**Chang'e-4** Pancam [14]	**Chang'e-3** Navcam [8]
FOV	25.5° × 19.1°	96° × 73°	38.3° × 38.3°	4.88° × 4.88°	46° × 46°	–
iFOV (µrad/px)	280	330	653	85	300–500	920
Baseline (cm)	24.08	∼ 42.5	–	–	∼ 27	∼ 27
Focal Length (mm)	26	∼ 10	14.67	38	100	50
Magnification	N/A	N/A	∼ 0.5x	∼ 0.3x	∼ 1x	∼ 0.4x
Detector Type	CCD	CMOS	CMOS	CMOS	CCD	CCD

TABLE 1.1: Key specifications summary of stereo cameras on Mars and lunar lander missions for planetary exploration

1.2.1 Limitations of Current Stereo Imaging Solutions

Upon reviewing existing stereo cameras used for lander application, several limitations were evident. These limitations points towards further advanced stereo imaging systems, designed for task-specific applications. Key challenges and trade-off to be taken into consideration for such designs are:

1. *Resolution vs. power*: The limiting factor of using a high resolution sensor lies in its power consumption. Even though a larger sensor format produces higher spatial resolution, they demand a significant amount of power and computational resources. This can be particularly challenging in power-constrained environments.

2. *Baseline length vs. size*: A key design element of a stereo camera is the distance between the two cameras, also known as baseline length. The distance is directly proportional to the working distance and space needed by the overall system. While improved accuracy for close range observation can be achieved by shorter baselines, a degradation of performance is observed with imaging objects in long range distances. A careful trade-off must be balanced depending the operational requirements for imaging tasks with near-range precision and far-range imaging capabilities.

3. *Environmental Challenges*: Imaging system performance is heavily affected by operational conditions, especially due to environmental factors. Variations in operating temperatures, lower illumination conditions, dust accumulation, etc. can all impact the resulting image quality of the camera and decrease its reliability. This particularly makes it difficult to operate remotely in harsh working scenarios.

4. *Mechanical and computational constraints*: Computational intensive real-time stereo matching poses another challenge in employing a high-precision imaging system. Such processing demands resource intensive on-board hardware to actively produces imaging products or transfer data to remote location. This introduces further constraints corresponding to size, power and thermal management in compact and resource limited platforms [3].

Following a trade-off study based on required performance and available resources, the proposal of a new stereo imaging system design aims to address these limitations while optimizing performance.

1.3 Problem Statement

The purpose of this project is to develop a prototype design of a stereo camera that addresses the limitations discussed above by introducing novel design elements. A practical and cost-effective approach is necessary which involves commercially available off-the-shelf (COTS) components, for easy and rapid prototyping of the camera system, while still ensuring the system compactness, and consistent quality of the stereo images captured. Table 1.2 outlines a set of predefined design requirements based on a potential rover mission scenario. In this scenario, the camera is mounted on top of the rover at a height of 250 mm above the ground and tilted at a 20° angle relative to the surface. The table outlines target spatial and depth resolution values, with a particular emphasis on achieving high resolution in the near range to inform the expected performance of the camera system.

Characteristics	**Description**
Depth of Field	200 mm
Spatial Resolution	150 µm/px
iFOV	500 µrad/px
Depth Resolution	1 mm/px
Cant Angle	20° (orthogonal)
Height above Surface	250 mm
Size	1U (10×10 cm)
Mass	400 g
Power	2 W

TABLE 1.2: Design requirements for the proposed camera

1.4 Objectives

The main objective of this project is to demonstrate the capability of a compact stereo camera to perform in-situ surface observations, allowing in-depth analysis without the need for sample return, thereby supporting real-time scientific investigations and operational decision-making during a mission. To achieve this, the design focuses on addressing the limitations of existing stereo imaging systems by introducing a novel monocular stereo approach. The system is built using a single detector and COTS components, ensuring compactness, reliability, and cost efficiency. The design is tailored to meet the specific operational requirements of a lunar rover, including a mounting height of 250 mm above ground and a 20° tilt angle relative to the surface, as outlined in the table 1.2.

The term "Lunar Lander" in the report title refers broadly to both stationary lander and mobile rover systems. For this project, the focus is on the rover application. The prototype design therefore addresses the specific challenges and operational needs of a lunar rover, ensuring it is well suited for dynamic movement and exploration on the Moon's surface [3].

1.5 Significance

The primary scientific application of the camera is the in-situ characterization of lunar regolith. Understanding the composition, texture, and physical properties of the regolith is crucial for a wide range of scientific and operational purposes, including resource utilization, mission planning, and geological studies. Traditional methods often rely on sample return missions, which are costly and time-consuming. By enabling high-quality stereo imaging, this compact camera system allows for remote, real-time analysis of surface features and material properties directly on the Moon. This capability supports more efficient scientific investigations and lays the groundwork for future autonomous exploration and in-situ resource utilization (ISRU) activities [3]. Monocular stereo cameras have not yet been deployed in lunar lander missions, making the development of such a system a significant step toward creating a versatile, compact scientific instrument tailored for photogrammetric-based in-situ experiments.

Previously flown stereo cameras for terrestrial exploration, especially on rovers, employed a binocular optic designs, having larger and bulkier sizes. With no moving component in the prototype design, this camera is able to capture the scene closer to the surface, and minimise power consumption, and is easier to operate. The scalability of the prototype design is of greater significance for task specific applications.

Adaptability of the size and viewing cone of the camera can be beneficial for lunar explorers, and can follow mission specific design requirements. By swapping all the components to state-of-the-art specifications, the camera can be utilised for various applications, apart from the ones mentioned in this report.

1.6 High-Resolution Stereo Imaging

In the field of computer vision, stereo vision is one of the direct ways to simulate how human eyes perceive real world objects in a 3D scene. It is achieved by imaging an object from multiple point of view, by either rotating or moving two cameras to satisfy the requirement. The reconstruction of a 3D object is carried out by extracting the 2D information from both images using the principle of triangulation. The disparity in the position of two image points x_l and x_r, for a corresponding real object point x in figure 1.1 is calculated from the stereo images as input. Resulting disparity can be converted to depth information of the target object with respect to the position of the camera [15].

1.6.1 Epipolar Geometry

The geometric relationship between the two cameras imaging the same object is defined by epipolar geometry. A pinhole camera captures an object on a 2D projected plane, hence the 3D positional information is not retained.

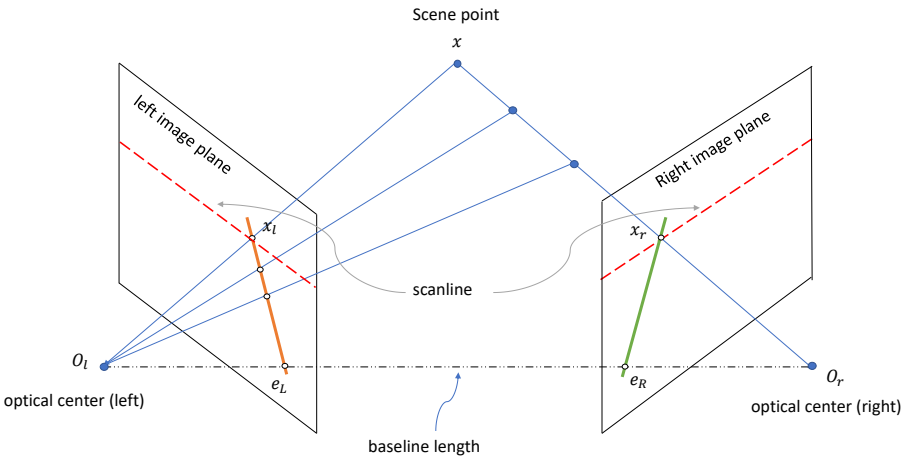

FIGURE 1.1: Schematic of epipolar geometry for stereo imaging

The epipolar geometry is defined by the epipolar plane, which passes through the 3D point being observed and the optical centres O_l, O_r of both virtual cameras. The intersection of this plane with the image planes of each camera forms the epipolar lines, shown as scanline in figure 1.1. Additionally, the epipoles e_L, e_R in figure 1.1, the points where the baseline (the line O_lO_r connecting the two camera centres) intersects the image planes, serve as the convergence points for all epipolar lines in their respective images. In certain configurations, the epipoles may lie outside the boundaries of the images, depending on the relative positions and orientations of the cameras. The epipolar constraint is advantageous as it ensures that the corresponding image point in stereo pairs lie on the same epilines. To mathematically describe epipolar geometry, two matrices are commonly employed: the Essential Matrix (E) and the

Fundamental Matrix (F). The Essential Matrix encapsulates the relative rotation and translation between the two cameras in a calibrated stereo system, relating the normalized coordinates of corresponding points. On the other hand, the Fundamental Matrix extends this relationship to pixel coordinates, incorporating the intrinsic parameters of both cameras [16].The Fundamental Matrix allows the mapping of a point in one image to its corresponding epipolar line in the other image, facilitating accurate feature matching and depth estimation [3].

Chapter 2

Methodology

2.1 State of the Art in Single-Detector Stereo Cameras

Photogrammetric imaging systems have mainly employed a set of cameras that image a scene in two different point of views at the same time or a single camera displayed by a small distance [17]. The main objective of using a single lens stereo imaging system is to reduce the complexity of the camera, and making it more suitable for deployment in dynamic surface environments, such as those encountered by rovers. These cameras often create difference in geometric and pixel intensities between the stereo images, making the process of stereo correspondence less accurate [17]. There have been many optical designs proposed for a single lens stereo cameras. Nishimoto and Shirai's system [18] has a rotating glass plate in front of the camera. The rotation of the plate simulates the parallel axes of two cameras by slightly shifting the optical axis at two different rotational positions. The resulting stereo images have easier point correspondence, although the depth map achieved is coarser. The camera structure developed by Teoh and Zhang [19] has geometry of two fixed mirrors in front of the camera at an angle of 45° with the optical axis of the camera. An additional rotating mirror is placed in between the fixed mirrors, such that it can rotate to position itself parallel with one of the fixed mirrors. Each position captures one of the stereo images at a time. Both of the above mentioned camera design successfully reduce the geometric and intensity difference in stereo images that are unwanted in a stereo camera system. However, the rotating element of the design poses a challenge in accurate movement of the parts. This creates a major design issue, especially when the stereo camera needs to be deployed in a non-static application.

Eliminating the moving part in such camera systems is essential to improve the opto-mechanical design of the stereo camera for rover application. Goshtasby and Gruver's study [17] solved this issue by proposing a design that obtains stereo images using a set of mirrors at an angle to the optical axis of the camera. The images are captured in a single shot by reflecting it along the axis of the mirror. Similar efforts were made by Nene and Nayar [20], by replacing the planar mirrors with non-planar reflecting surfaces such as ellipsoidal, hyperboloid and paraboloid mirrors. A wider field of view was achieved with the camera design, although the complex mirror mechanism made it difficult to replicate the design.

Another novel and practical stereo camera system was proposed by Lee and Kweon [21], wherein a biprism is placed in front of the camera to obtain a stereo image on a single detector. The biprism was designed in a way that the left and right stereo image were projected on two halves of a single detector. Unlike prior mentioned designs, they not only removed any moving element, but also made it easier to calibrate and cheaper to build. Taking advantage of the geometric setup, the point correspondence between the two stereo images was simplified, as they automatically lie on a single scan-line.

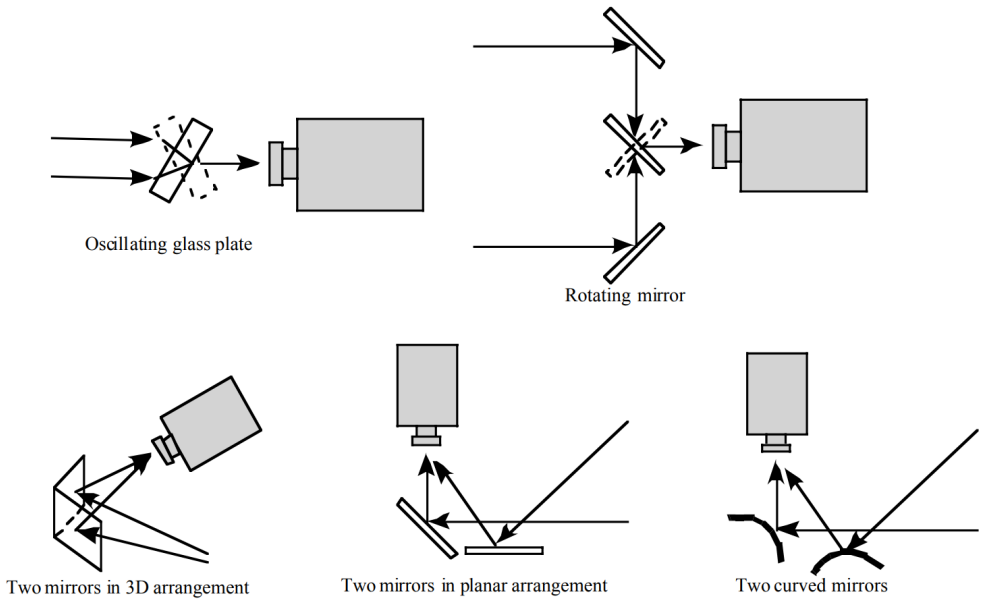

FIGURE 2.1: Optical configuration of various stereo cameras using a single detector [1]

.

Some limitations of this design include a smaller field of view and availability of the desired biprism in the commercial market.

As described in Goshtasby and Gruver's study [17], an ideal stereo camera system employing a single detector, must possess certain properties to create reliable and accurate stereo images for 3D reconstruction. These include:

1. The object must be imaged using only one lens in single shot and without any time delay between two images' acquisition.

2. The stereo camera must have the ability to adapt its field of view as needed for different applications.

3. Stereo image pair must contain no geometric and intensity differences between images, that could introduce discrepancies and errors during stereo processing.

4. Stereo images are produced in a way that the corresponding object point occurs on the same scanline for effective stereo matching.

2.1.1 Proposed Design of Single-Detector Stereo Camera

To fulfil the design requirements of the stereo camera for a lunar lander, an adapted optical design must be implemented. This design is best suited due to its cost-effectiveness, system compactness and availability of components from the commercially available off-the-shelf market. The most popular single-camera stereo systems, amongst various other pseudo-stereo imaging systems, is the one using a four-mirror adaptor [22]. Significant development have been made to design such stereo systems, as it offered diverse applicability, reduced image distortion and variable field of view. The first attempt was made by Pankow and Besnard [23, 24], to combine a four-mirror assisted single-camera stereo system with the method of digital image correlation (DIC) for application in experimental mechanics.

Component	Description	Quantity
Detector	1.6 MP CMOS (monochrome)	1
Lens	focal length: 16 mm, f/#: 1.8 - 22	1
Inner mirrors	right-angle reflective prism, 25 mm × 25 mm reflective legs	1
Outer mirrors	50.8 mm square protected silver mirror, 3.2 mm thick	2
Mirror Adaptor	3D printed	1

TABLE 2.1: List of commercially available components used for the camera setup

In this study, a single detector, four-mirror assisted stereo camera is constructed based on Luo's study [22] for the optical design and comprehensive calculation of geometric parameters are discussed in the next section.

2.2 Opto-mechanical Design and Development

A robust and efficient stereo camera system which meets the previously outlined requirements is needed for the practical application. To achieve this, the methodology of determining vital input parameters involves several key steps: analytically determining the appropriate camera specifications, geometrically designing the mirror adaptor, selecting optimal components, and finally breadboarding and assembling the resulting camera setup.

2.2.1 Input parameters

The design process is initiated with the identification of essential input parameters, mainly derived from pre-defined design requirements and optical components based on availability. These parameters includes sensor size (H_s), viewing angle of the camera (θ), required spatial resolution (ξ_{image}), and depth resolution (δ_z), establishing the precision needed for accurate depth measurement. Utilising a monochrome CMOS detector from Thorlabs, a 1/2.9" format, 1440 × 1080 pixel (1.6 MP) sensor with 3.45 µm square pixels, defines the dimension of the imaging sensor. Additionally, the height of the stereo camera (H_t) above ground is predefined to be at 250 mm, as it designed to be mounted on top of a lunar rover. The orthogonal viewing (cant) angle (θ) of the camera located in front of the rover is set to be 20°. These parameters will highly influence the field of view (FOV) and working distance (W_{d_1}) of the camera setup.

The working distance (W_d) is the range of space in front of the camera, over which the lens can focus and get sharp images. With the help of simple trigonometry, the working distance for the nearest object in focus is given by:

$$W_d = \frac{H_t}{\cos(\theta)} \tag{2.1}$$

where θ is the orthogonal viewing angle in degrees, and H_t is the height above ground in cm.

The size of a camera sensor's active area is referred to as sensor size. The sensor size (H_s); horizontal or vertical, can be directly calculated from the pixel size (P_s) and number of active pixels on the sensor (P_c) as:

$$H_s = \frac{P_c}{P_s} \tag{2.2}$$

The FOV is defined as the viewable area in the object space that can be imaged by a camera system. Best described as horizontal or vertical FOV in mm, or an angular field of view ($AFOV$) in degrees, the relationship 2.3 is calculated from the input parameter already known:

$$FOV = \xi_{image} \cdot P_c \tag{2.3}$$

2.2.2 Camera Parameters

With the help of input parameters, the critical camera specific parameters can be derived. One of the key camera specifications is system magnification (m). To determine the absolute minimum resolvable spot viewable on the object, the ratio of the field of view (FOV) to the sensor size (H_s) can be calculated as:

$$m = \frac{H_s}{FOV} \tag{2.4}$$

System magnification scales the image space resolution up to the object space resolution (ξ_{object}).

$$\xi_{object} = \xi_{image} \times m \tag{2.5}$$

Another fundamental camera parameter is focal length (f) of the system as it describes how strongly it can diverge or focus light onto the imaging plane. The objective of this camera system is to achieve high resolution images, hence a wider FOV is compromised. To achieve the desired FOV, the focal length (f) is calculated as:

$$f = \frac{H_s \times W_{d_1}}{FOV} \tag{2.6}$$

For a fixed focal length lens, the angular field of view ($AFOV$) is also finite. The camera can be focused on objects at different working distances, with varying FOV, while maintaining a constant viewing angle. A typical full angle associated with the width of sensor (H_s) used, is specified as $AFOV$. From this definition, ($AFOV$) can be calculated as:

$$AFOV = 2 \times \arctan\left(\frac{H_s}{2f}\right) \tag{2.7}$$

Similarly, the instantaneous field of view ($iFOV$), which is the field of view of a single pixel can be calculated in μrad as:

$$iFOV = \frac{P_s \times 1e6}{f} \tag{2.8}$$

The ability of a lens to maintain a desired image quality without refocusing is known as depth of focus (DOF_o) of the camera. It ultimately measures the tolerance in positioning of the image plane in relation to the lens, and maintaining the acceptable sharpness of the acquired images. To measure and capture objects with finer details, a small depth of focus is required to obtain high image resolution, which can be calculated as:

$$DOF_o = \delta_z \times m^2 \tag{2.9}$$

The effective spatial resolution produced by the camera system is heavily influenced by parameters like depth of field, f number ($f\#$), and sensor size (H_s). When imaging a point source object, the objective lens used in this camera setup does not focus all the

light rays perfectly, as an ideal lens would. This creates a blurry spot instead of a point on the image plane, and the diameter of this disk is included in the design process, namely circle of confusion (CoC). Here it is assumed to be equal to actual pixel size. The required f number ($f\#$) can be derived for selected depth of field. This parameter determines how much light enters the lens and ends up on the imaging plane:

$$f\# = \frac{DOF_o}{2 \cdot CoC} \tag{2.10}$$

The aperture diameter (ϕ_A) is given by:

$$\phi_A = \frac{f}{F_n} \tag{2.11}$$

To derive the effective depth of field of the camera system, the range of distance to the object from the camera is to be determined where the image have an acceptable sharpness. Hyperfocal distance, near distance of acceptable sharpness, and far distance of acceptable sharpness are calculated using the following equations [25]. The hyper-focal distance (H_f) is calculated as:

$$H_f = \frac{f^2}{F_n \times CoC} + f \tag{2.12}$$

The nearest distance of acceptable sharpness (D_n) is given by:

$$D_n = \frac{W_d \times (H_f - f)}{W_d + H_f - 2f} \tag{2.13}$$

The farthest distance of acceptable sharpness (D_f) is:

$$D_f = \frac{W_d \times (H_f - f)}{H_f - W_d} \tag{2.14}$$

The obtained depth of field (DOF_c) is:

$$DOF_c = D_f - D_n \tag{2.15}$$

The stereo baseline length (B) for the farthest object in focus is:

$$B = \frac{P_s}{f} \times \frac{W_{d_2} \times (W_{d_2} + \delta_z)}{\delta_z} \tag{2.16}$$

where δ_z is the desired depth resolution.

Although the camera is initially designed based on the requirement for lunar rover mounting, it is also adaptable for lander platforms, enabling high-resolution stereo imaging for descent, hazard detection, observing lander-surface interaction. In this report, the focus is placed on the rover application of the camera, as it presents a broader range of operational scenarios and mobility-based imaging requirements. However, it is important to note that the design remains flexible and can be tailored to meet the specific needs of particular mission profiles, depending on the scientific objectives and mission constraints [3].

2.2.3 Stereo convergence

Conventional stereo cameras employing a binocular lens system typically feature optical axes that are either parallel, converging, or diverging. The configuration of the optical axes is determined based on the required FOV and depth of field that the system must achieve, with the design carefully tailored to include the appropriate rotation of the optical axes. In parallel-axis stereo cameras, corresponding object points in the stereo images generally lie on the same scanline, which simplifies stereo processing. However, in systems where the optical axes converge or diverge, the corresponding object points do not naturally align along the same scanline. To address this issue, mathematical relationships are formulated and applied to transform the stereo image points, ensuring alignment along an identical scanline. This transformation mimics the behaviour of parallel-axis configurations for efficient stereo processing [3, 17].

To achieve the desired FOV with the calculated convergence of the optical axes, the baseline length of the stereo camera system is determined. It is essential, however, that the optical axes of both cameras are maintained within the same horizontal plane. This helps in eliminating any misalignment, which would otherwise result in discrepancies between the stereo images and complicate feature matching processes. For single-detector stereo cameras, the optimal convergence of the optical axes is a critical aspect of design and is carefully determined based on a trade-off between depth of field and FOV requirements [3]. The design must account for how the optical components are configured to replicate the convergence angle accurately as per the calculated specifications in section 2.2.2.

Proper alignment depends significantly on the precise placement of the mirror pair and the internal prism reflector. Any misalignment of these components can introduce distortions in the stereo images, which negatively affect the quality and reliability of stereo matching. Such distortions undermine the ability of the system to produce accurate depth and spatial measurements, highlighting the importance of meticulous optical alignment in the design and implementation of stereo camera systems [3].

2.2.4 Optical Simulation

To simulate the optical system, optical simulation software Ansys® Zemax OpticStudio was used to replicate the physical configuration and analyse the system's performance, as illustrated in figure 2.2 [26]. The object space, corresponding to the calculated FOV, is positioned in front of the optical components at a distance that approximates the estimated working distance of the system. The arrangement of mirrors and the reflective surfaces of the prism are modelled to closely match the geometry of the actual camera setup, ensuring accurate representation of the optical path and alignment.

The lens objective in the simulation is modelled as a paraxial lens, which assumes ideal optical properties with no aberrations. This simplification allows for a clearer analysis of the system's fundamental performance by eliminating the complexities introduced by real-world optical imperfections such as spherical aberration, chromatic aberration, and diffraction effects [27]. The focal length and aperture of the paraxial lens are chosen to match the specifications of the actual objective used in the physical system, ensuring that the simulated results remain representative of the real-world optical behaviour [3].

To keep the simulation clear and simple, the model includes only one of the two symmetrical optical paths for the virtual cameras. This camera is configured to image onto half the width of the detector, effectively representing one side of the full imaging

system. This approach reduces complexity while still providing effective performance of the optical system.

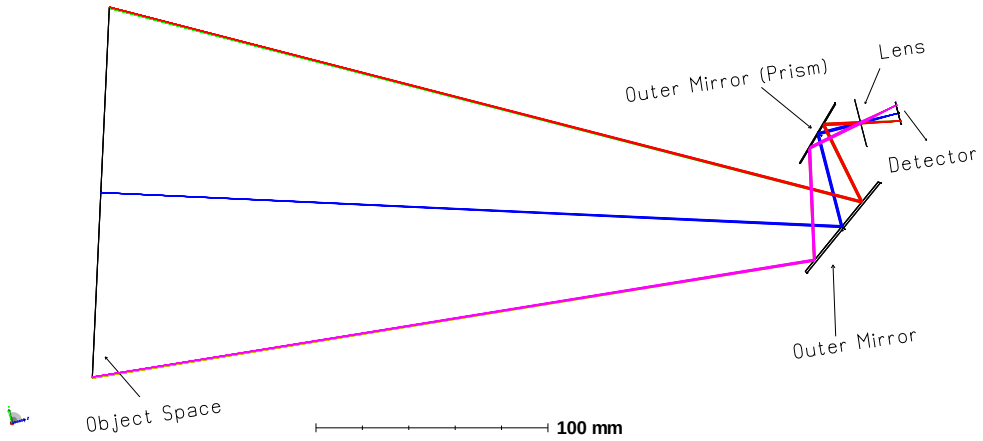

FIGURE 2.2: Optical path and components in a simulated camera system

Figure 2.3 presents the diffraction-limited Modulation Transfer Function (MTF) computed using the Fast Fourier Transform (FFT) method. The MTF is a critical metric for evaluating the resolution and contrast performance of an optical system, representing the system's ability to transfer spatial frequency information from the object to the image plane [28].

In this simulation, the optical setup is configured to model a square wave object with a specified spatial frequency. The FFT-based MTF calculation involves propagating the wavefront through the optical system and computing the intensity distribution at the image plane using Fourier optics principles [28].

The MTF curves are generated for two key field points: the centre and the corner of the image plane. This allows for an assessment of the system's performance across the FOV, which is particularly important for applications requiring uniform resolution. The analysis is conducted over a wavelength range of 400 nm to 700 nm, simulating broadband visible light conditions. Additionally, effective aperture of the lens is considered to be F16.0 in the simulated setup for the purpose of ease. The resulting MTF plots illustrate the modulation response as a function of spatial frequency in image space, depicting the optical system's imaging capabilities under different field and spectral conditions [3]. The spatial frequency where MTF value is about 50% is realised at 52 lp/mm at image corner and 56 lp/mm at image centre. Such analysis showcases the uniformity of the image space resolution throughout the imaging plane, and helps evaluate the performance of the camera system in a simulated environment. Translating the spatial frequency in line pair per millimetre into object space resolution results in a range of 142 μm to 153 μm per pixel.

2.3 Measurement Principle and Procedure

After a successfully established optical design of the stereo camera, the next steps involves the implementation of the stereo image processing pipeline to extract the depth information from the acquired stereo images. This section outlines the measuring principle and procedure used to accurately derive depth maps. A lunar regolith

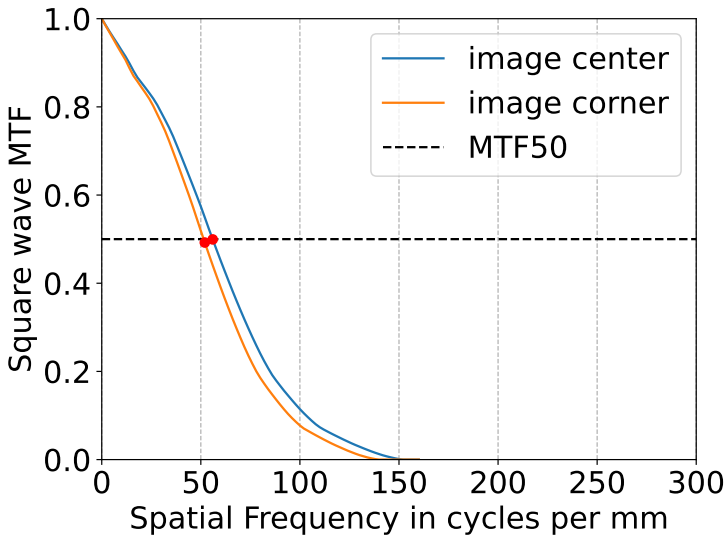

FIGURE 2.3: Polychromatic diffraction MTF curve for square wave response from simulated optical system. The curve illustrates the system's contrast transfer performance across spatial frequencies.

simulant EAC-1A sample was selected as the target object image acquisition and subsequent stereo processing [29]. The practical stereo vision system consists of mainly six modules for successful extraction of depth information of the target object:

2.3.1 Image acquisition and Pre-processing

The first step of the image processing pipeline is capturing the target scene with the stereo camera. An image acquisition application ThorCam™ Software for Scientific and Compact USB Cameras is used [30]. Single images and image sequence can be captured by communicating with the camera via the graphical user interface. The application provides a direct control over the camera configuration, image acquisition and reviewing. The object is placed in the field of view of the camera and resulting stereo images are acquired.

The camera is designed in a way that images from the virtual camera are received by a single detector. Hence the resulting images acquired need to be dissected into two separate images in order to further process it as stereo image pair. An automated pre-processing sequence was generated in Python, to load the raw images, and extract the stereo image pair.

Additional steps were carried out to improve image quality and enhanced to effectively highlight the features that might be easier for the algorithm to detect for stereo matching. To enhance the contrast of the regions in image, with limited illumination in shadowed objects, Contrast Limited Adaptive Histogram Equalization (CLAHE) algorithm is implemented to make the feature extraction more accurate. This algorithm can operate on a small dataset and works effectively on smaller regions, making it a suitable choice for this application [31].

Figure 2.4a is the raw image with both left and right view as seen by the sensor. After enhancement, the features are more prominent with increased contrast of the object in the shadowed region of the lunar regolith simulant pile shown in figure 2.4b.

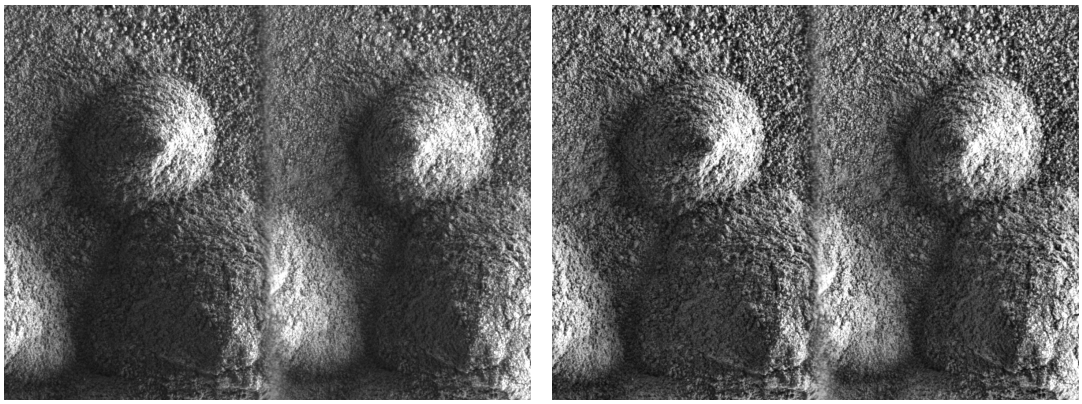

(A) Unprocessed stereo image pair captured at the detector, showing the original scene without any image enhancement or preprocessing applied.

(B) Stereo image pair after contrast enhancement using the CLAHE (contrast-limited adaptive histogram equalization) algorithm for improved contrast.

FIGURE 2.4: Comparison between the original and contrast-enhanced stereo image pairs.

2.3.2 Geometric Camera Calibration

To ensure precise measurements and reliable analysis of the 3D information of the object, it is necessary to carry out an accurate calibration of the camera [15]. Every stereo vision algorithm works on the principle of finding the depth of pixel from image coordinates into 3D world coordinates. This process is known as backward projection of a camera. The mathematical relationship between object point in three-dimensional space and its corresponding image point, projected on the image plane is described by Maamir and Haghi [32], also known as forward projection model. Following the pinhole camera model, this model assumes that the camera aperture is point and light is focused without any lens for simplification.

It also assists in obtaining intrinsic and extrinsic parameters of the camera in the form of the camera matrix (P) [33]. The correspondence between the image and object coordinates can be accurately established with these matrices:

$$P = K \begin{bmatrix} R & t \end{bmatrix}$$

1. Intrinsic matrix (K): It facilitates mapping between pixel coordinates and camera coordinates in the image frame resulting in internal parameters such as optical centre, focal length, and radial distortion of the lens indicated by the matrix elements. The intrinsic matrix is defined as:

$$K = \begin{bmatrix} f_x & s & c_x \\ 0 & f_y & c_y \\ 0 & 0 & 1 \end{bmatrix}$$

   where, $\begin{bmatrix} c_x & c_y \end{bmatrix}$ are optical centre in pixels, (f_x, f_y) is the focal length in pixels, and s is the skew coefficient constant, which accounts for non-perpendicular image axes.

2. Extrinsic matrix $\begin{bmatrix} R & t \end{bmatrix}$: The extrinsic parameters describes the location and orientation of the camera in a 3D world coordinates in the form of rotation (R), and a translation (t).

3. Distortion coefficients: As the camera configuration follows the pinhole camera model, lens distortion does not play a significant role due to lack of the lens in an ideal pinhole camera scenario.

Zhang [34] introduced a new calibration method in 2000, wherein a calibrated pattern of a known geometric shape was used. Illustrated in figure 2.5, a chessboard pattern with known dimensions is used to get multiple calibration images, with varying distances and orientation with the imaging plane. These images acts as an input for the camera calibration toolbox for MATLAB application [33].

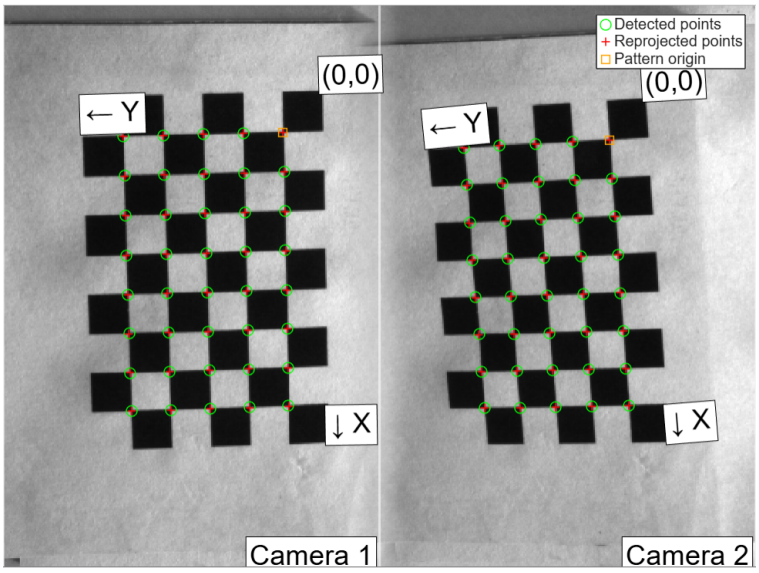

FIGURE 2.5: Detected chessboard pattern in calibration images using MATLAB stereo calibrator toolbox. Camera 1 and Camera 2 relates to left and right camera respectively

Parameters	**Left camera**	**Right camera**
Focal length (pixels)	$[4521, 4535]$	$[4577, 4538]$
Principal point (pixels)	$[646, 348]$	$[676, 535]$
Skew	$[14]$	$[-26]$
Radial distortion	$[-0.26, -27, 749]$	$[0.92, -131, 363]$
Tangential distortion	$[0.01, -0.018]$	$[0.003, -0.002]$

TABLE 2.2: Intrinsic matrix calculated with camera calibration toolbox

Parameters	**Left camera**	**Right camera**
Rotation vectors	$[0.01, -0.15, 1.54]$	$[0.31, 0.08, 1.5]$
Translation vectors (mm)	$[-7.12, -6.83, 295]$	$[-15, -18, 304]$

TABLE 2.3: Extrinsic matrix (position and orientation of right camera relative to left camera)

The calibration parameters mentioned above were used to remove distortion from the images and rectified images can be calculated. However, for the actual stereo processing pipeline, an uncalibrated rectification approach is used. This eliminates the need to perform the detailed geometric calibration steps discussed in this section.

The geometric calibration process is carried out primarily as a validation step, to compare the calculated camera parameters with the actual realised values.

2.3.3 Image rectification and feature extraction

The next step of the image processing is to detect feature points and obtain accurate correspondence between the stereo images. When the extrinsic parameters like focal length and baseline length are known, an uncalibrated 3D reconstruction can be performed with the help of various feature matching algorithms. This method helps to rectify the stereo images, without needing to perform calibration with a calibration pattern of known dimensions. A stable and robust feature extraction algorithm is used, which also performs well in the variable environment of the lunar surface. Several feature extraction algorithms have been developed for computer vision systems for tasks like object recognition, image matching, and scene understanding [35]. The simplified inverse filter tracking (SIFT) algorithm has been identified as the most effective algorithm for feature point extraction [36]. It is well suited for the application of a lunar rover, due its invariance to change in illumination, image noise, scaling, rotation, and minor viewpoint differences [35]. The key steps of the algorithm in feature extraction and stereo matching, as described by Lowe [37], are:

1. Keypoints are identified across stereo images by comparing each pixel with its neighbouring pixels as shown in figure 2.7.
2. Then, it determines a precise location of the pixel point, refines keypoints by fitting each keypoint to their model and rejects those with low contrast and poorly localised feature edges.
3. To ensure its invariance to image rotation while detecting feature points, each keypoint is assigned several orientations with reference to local image position.
4. Finally, a feature vector descriptor is defined for each refined keypoints, further utilised for stereo matching between corresponding stereo images.

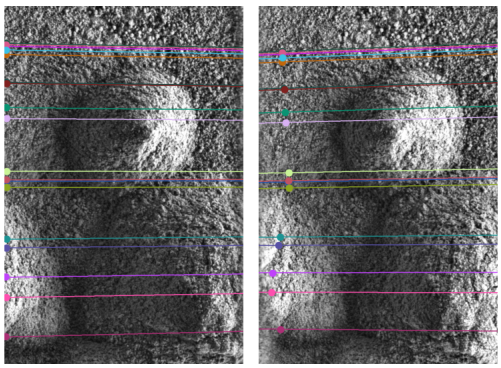

(A) Epipolar lines in the stereo image pair before rectification, with circular markers indicating feature matches detected between the left and right images. The non-parallel orientation of the lines reflects the un-rectified geometry.

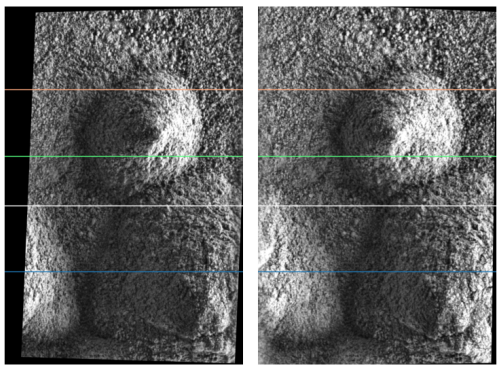

(B) Epipolar lines after image rectification. The lines are approximately parallel, demonstrating successful alignment of the image planes for simplified stereo matching

FIGURE 2.6: Feature matching based image rectification results of stereo images

Epipolar geometry represents a geometric relationship between observed images with the 3D structure of the target. It combines the 3D points of the object and their

image projections, enabling a 3D reconstruction of the target object observed from a multiple viewpoints [38]. Epipolar geometry follows the principle of the pinhole camera model, resulting in epipolar constraint commonly used in stereo matching methods [35]. For each feature point, the best matching point candidate is located in its corresponding epiline. By the means of image rectification, the complexity of feature correspondence between the stereo images can be reduced, and limiting the search space to one dimension. Image rectification essentially aligns the left and right images in a way that the search window is in the same pixel line. This results in a confined search space and improves the computational time and accuracy of feature detection.

Figure 2.6 shows the original stereo image pair with epilines, before and after rectification. The epilines for the rectified images indicate that the epipolar lines corresponding to each feature are parallel, thus removing the vertical disparity between the stereo pair.

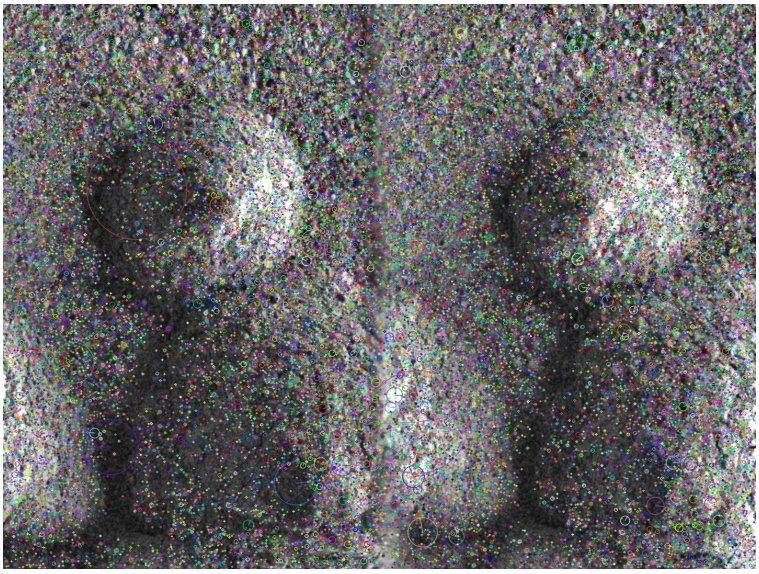

FIGURE 2.7: Keypoints detected in the contrast-enhanced stereo image pair using the SIFT (scale-invariant feature transform) algorithm. The detected points represent similar features suitable for stereo matching and 3D reconstruction.

2.3.4 Stereo matching

To create a dense 3D reconstruction of the target scene, the preferred method for stereo matching is usually based on correlation between neighbouring pixels. The SIFT features are used to perform stereo matching, by combining the pixel location in an image space coordinates system. The OpenCV python package offers an effective and simple to use stereo matching function: the Semi-Global Block Matching (SGBM) adapted from Hirschmuller's [39] stereo processing algorithm [31]. A sliding search window block computes the similarity between the pixels around the region of interest. The pixel corresponding to an object point between the stereo image pair with highest similarity is calculated by pixel-wise matching costs across the region. This algorithm assumes that the intrinsic and extrinsic orientation of the camera is known. This method performs effectively with textureless regions, geometric occultations and radiometric differences in stereo images. Instead of employing a 2D global cost computation across the entire image, this approach computes it for a single row of

pixels, reducing it to a 1D search constraint. Aggregating multiple costs for each pixel along all paths radiating from the pixel, ensures smoothness of the results along with preserved local details. Additional smoothness constraints are employed by penalising the change in disparity between neighbouring pixels. This enforces smoothness by applying a small penalty for slight disparity changes, and a larger penalty for drastic disparity changes such as at the object boundaries [39].

2.3.5 3D information extraction

In order to obtain 3D information of the imaged scene, disparity (D) needs to be calculated for each pixel of the image. The disparity with minimum aggregated cost is selected to create a dense disparity map. Based on the epipolar geometry, disparity corresponds to the horizontal shift between matching pixels between the stereo images. With the help of triangulation, the distance of an object point from the camera is inversely proportional to the disparity of the object point. This implies that the farther the object is from the camera, the lower the value of disparity for the corresponding pixel in stereo images.

Considering a camera with converging optical axis, the depth information of a point in scene can be calculated with geometric calculation from Goshtasby and Gruver's study [17]. Assuming that the focal length (f), baseline length (B), tilt angle of the left and right mirrors (α_t), and distance between the camera centre and mirror's common axis (d) is known, the depth of the object point (Z) is given as:

$$Z = \frac{fB}{D - (x_l - x_r)} + \frac{B}{2(sin2\alpha_t)(1 + cos2\alpha_t)} \tag{2.17}$$

where (x_l, x_r) are coordinates of the point where the principal ray from the origin of world coordinate system, intersects with the image plane.

This results in the map of depth values at each pixel with world coordinate system. Equation 2.17 is based on the pin-hole camera model, and computes the geometric relationship between the stereo camera and the 3D information of the scene observed.

2.3.6 Image post-processing

Inconsistencies and noise in results are inevitable in vision based image processing. However, the Semi-Global Block Matching (SGBM) algorithm is robust and computationally efficient in generating disparity maps [31]. Further refinement is necessary to enhance the quality and reliability of the disparity maps. To achieve a more accurate and visually coherent disparity map, the SGBM parameters are carefully fine-tuned, namely:

1. *Block Size*: Determines the size of the matching window. A larger block size improves robustness in low-texture regions but may reduce detail. A smaller block size enhances fine detail but is more sensitive to noise. A block size of 5–11 is typically used for a balance between accuracy and performance.

2. *NumDisparities*: Defines the range of possible disparities to search. A higher value increases accuracy but also computational load. It is usually set to a multiple of 16 to align with hardware optimizations.

3. *UniquenessRatio*: Controls the uniqueness of the best match. A higher value increases confidence in the match but may result in missing valid disparities in inconsistent regions. A typical value is between 5 and 15.

4. *Speckle Filtering Parameters (SpeckleWindowSize and SpeckleRange)*: These parameters help remove small, noisy regions (speckles) in the disparity map. A larger window size and range allow for more aggressive filtering, improving smoothness at the cost of detail. Typical values are 100–200 for window size and 1 to 4 for range.

By adjusting these parameters based on the specific characteristics such as texture, lighting, and scene complexity of the stereo image pair, it is possible to significantly enhance the quality of the disparity map [3].

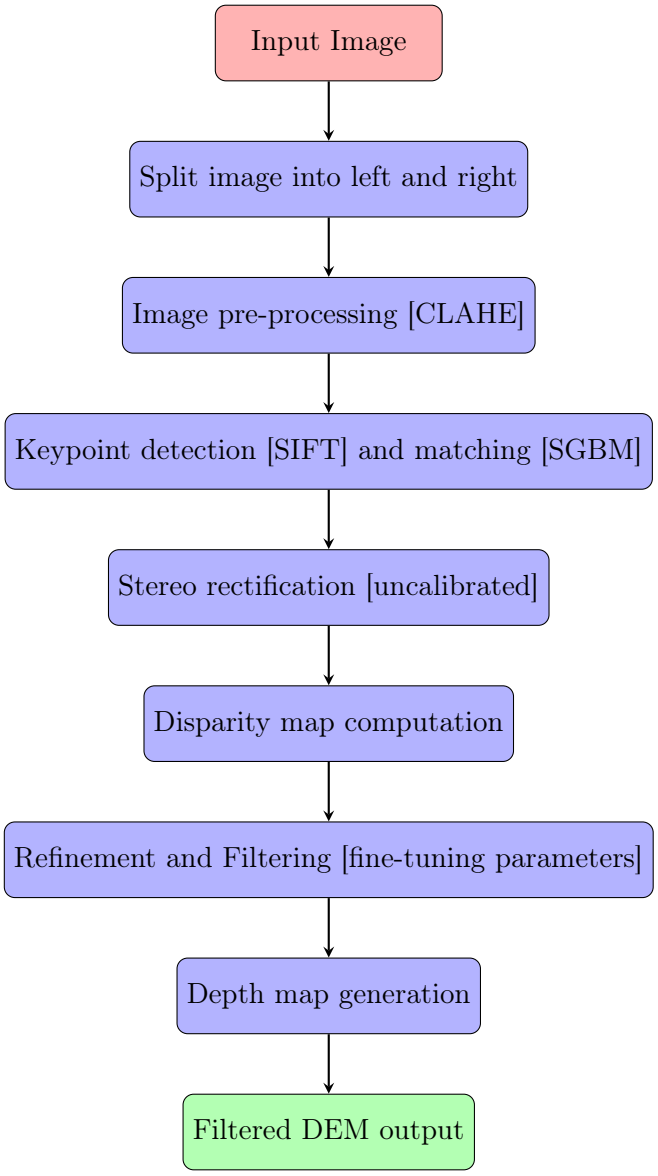

FIGURE 2.8: Flow diagram representing the stereo image processing pipeline

Chapter 3

Experimental Setup

3.1 Breadboarding and Initial Tests

The main design and performance objectives that are realized by the optical design of the stereo camera are:

1. Achieving stereo imaging capabilities using a single detector, while adhering to compact size constraints, specifically a 1U form factor with a mass less than 400 g and 1 W power consumption.

2. High-resolution photogrammetric analysis of the immediate lunar surface in proximity to the lunar lander, achieving a spatial resolution of < 150 micrometers per pixel.

3. Obtaining precise depth resolution of up to 1 millimetre to support detailed surface characterization.

To demonstrate the effectiveness of the designed stereo camera system in generating accurate stereo images, a stable breadboard plate on a optical bench was used to construct an experimental camera setup is shown in figure 3.1. The breadboard plate provide a rigid platform for mounting the optical components, ensuring an accurate alignment and minimized external vibration of the setup. The imaging system comprises of a 3D-printed four-mirror adaptor as the core optical component, designed to house and precisely align the optical mirrors for accurate redirection of the light path. Constructed with durable material, the adaptor provides a compact and stable frame, maintaining its structural integrity [3]. Custom designed to incorporate mount and compartments, the adaptor securely holds the mirrors in orientation predefined by the design, and accurately aligns the FOV of the camera. The adaptor integrates a right angle mirrors prism, featuring reflective coating to both of the legs, redirecting the incident light at a precise 90° angle. The reflective surfaces, with dimension of 25 mm $\times$ 25 mm each, provides a clear aperture without introducing significant aberrations, contributing to the high-resolution and compact design of the camera. As first surfaces of this optical system, a pair of aluminium coated, 508 mm wide square mirrors are employed, placed in the corners of the adaptor. Each mirror acts as the first point of light ray contact for both left and right camera views respectively. These mirrors exhibit average reflectance in excess of 90% across the 450 nm to 2 µm wavelength range.

A Cinegon 1.8/16 - ruggedized megapixel lens, with an adjustable aperture ranging from 1.8 - 16), and a focal length of 16 mm is used. The lens is corrected and broadband-coated for the spectral range of 400 nm – 1000 nm (VIS + NIR), making it suitable for a wide variety of lighting conditions. These components were mounted securely in front of the entrance pupil of the four-mirror adaptor, allowing for optimal control to adapt the depth of field and light gathering ability in various imaging

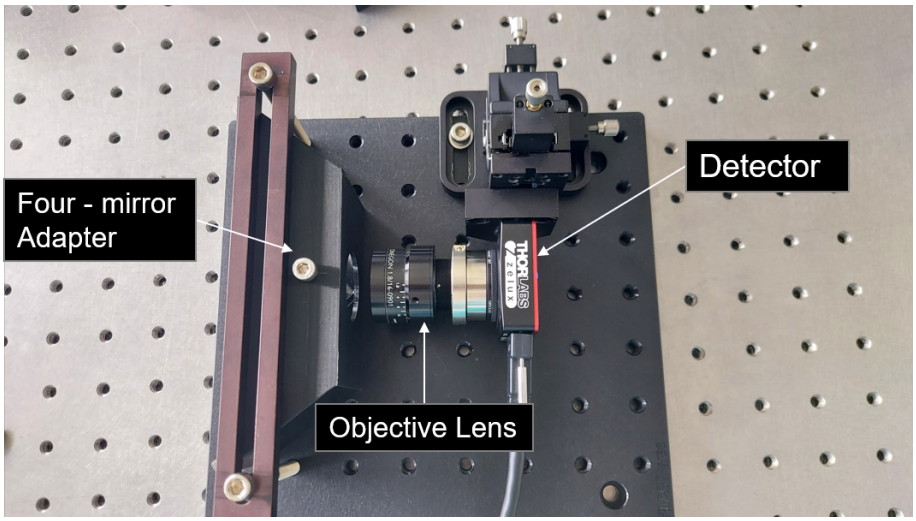

FIGURE 3.1: Image of the experimental setup, illustrating the breadboarded optical including the detector, objective lens and four-mirror adaptor, used for testing the stereo imaging.

conditions. As the imaging sensor, Thorlabs Zelux® 1.6 MP monochrome CMOS scientific digital camera was employed. Delivering high resolution data capture with its 3.45 µm × 3.45 µm square pixels, this sensor provides a total imaging area of 4.968 mm × 3.726 mm, ensuring fine detail preservation. With adjustable exposure time in fine increments of 0.025 ms, and a global shutter mechanism, it provides a distortion free image of fast moving scenes. The sensor is powered via USB, consuming only 1.17 W under operation, and is designed to function optimally within an ambient temperature range of 10°C to 40°C. The mirror adaptor is clamped with the help of screws and the mirror pairs are placed as shown in the figure 3.3. The mounting of the proposed camera system on top of the rover assumes a canting angle (θ) of 20° from the orthogonal axis. The camera positioned at a height (H_t) of 250 mm above the lunar surface. This predefined configuration has been replicated in a laboratory setting to simulate field conditions, as illustrated in figure 3.2.

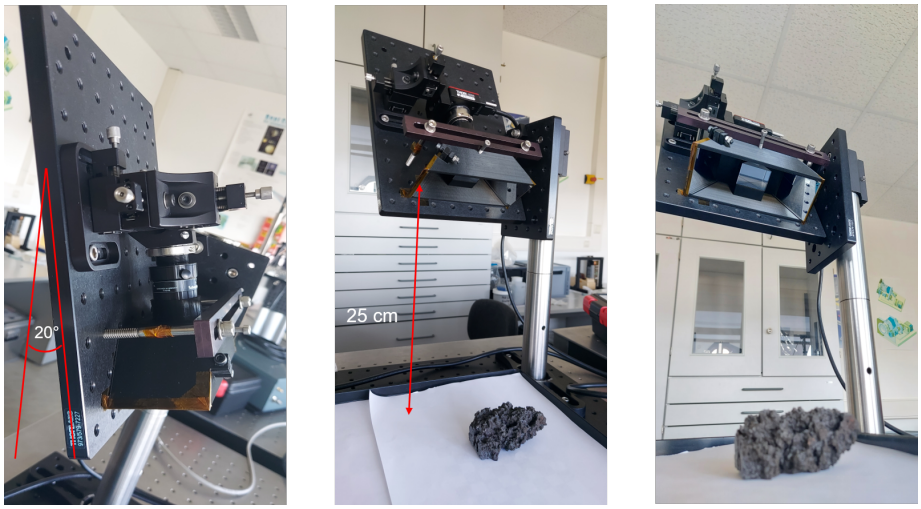

FIGURE 3.2: Image showing the camera mounted on a simulated rover setup at a height of 25 cm above the surface with a 20° cant angle, directed toward a basaltic rock sample for stereo imaging.

Camera parameter	**Description**
Detector	Monochrome CMOS
Active Imaging Area	4.968 mm × 3.726 mm
Pixel Size	3.45 μm (square pixel)
Effective Working Distance	260 mm - 310 mm
Effective Focal Length	16 mm
Aperture (f/#)	16
FOV	52 mm × 80 mm
Effective Stereo Baseline	116 mm
iFOV	601 μrad/px
Magnification	0.063
MTF	$>$ 0.45 at Nyquist
Size	120 mm × 150 mm
Weight	460 g
Power	1.17 W

TABLE 3.1: Derived camera specifications after the design phase

The controlled laboratory setup ensures an optimal alignment of the components for the intended FOV calculated with equation 2.3. The cant angle of 20° is considered an integral parameter to the system's design. Applying this configuration, the topmost pixel rows of the detector can image objects up to 266 mm with acceptable sharpness in front of the rover, as defined in equation 2.13, while the bottommost pixel rows can image distance up to 311 mm, as defined in equation 2.14. The performance requirements necessary for both experimental validation and field application are realised with this setup.

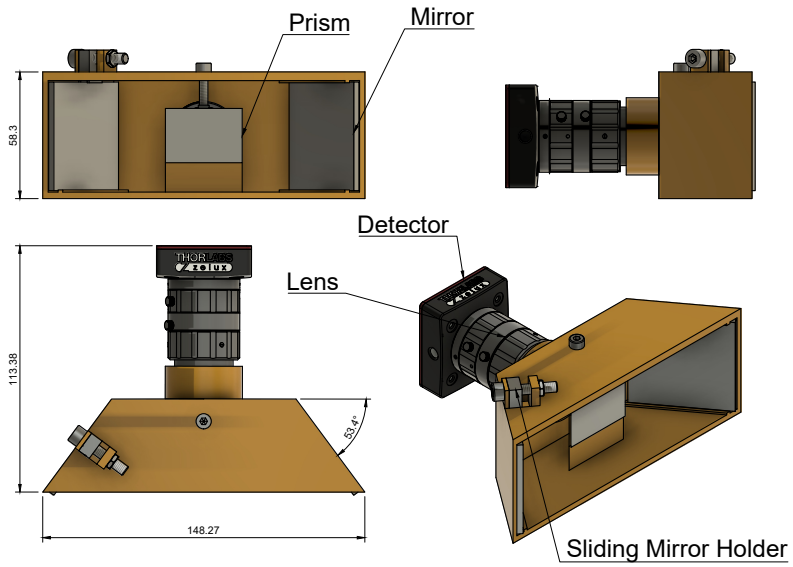

FIGURE 3.3: 3D CAD model depicting the spatial layout of the stereo camera.

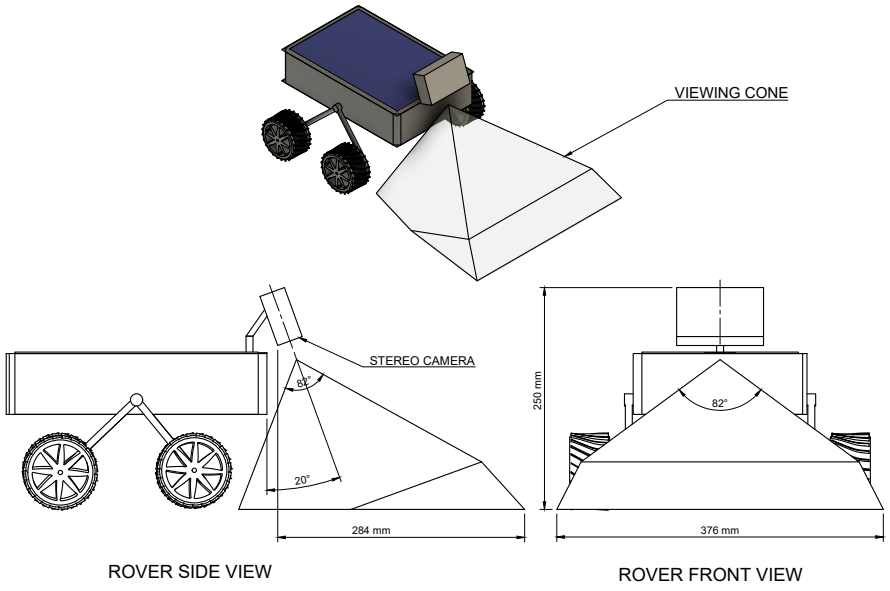

FIGURE 3.4: Illustration depicting orientation and coverage of viewing cone of the stereo camera, when mounted on top of a rover

3.2 Stereo Imaging Results

The stereo imaging process is initialised by capturing a scene, with two separate perspectives, simultaneously at different viewing angles. This introduces disparities in position of the corresponding pixel on an object point, in the left and right images. This disparity detection is essential in accurate 3D reconstruction and depth estimation of the scene. The disparity map is a greyscale image, where the intensity of each pixel represents the disparity value between the stereo image pair. Brighter pixel values corresponds to higher disparity values and vice versa. This indicates that the object closer to the camera will have brighter pixel values or higher disparity values, following the triangulation principle mentioned in section 1.6.1.

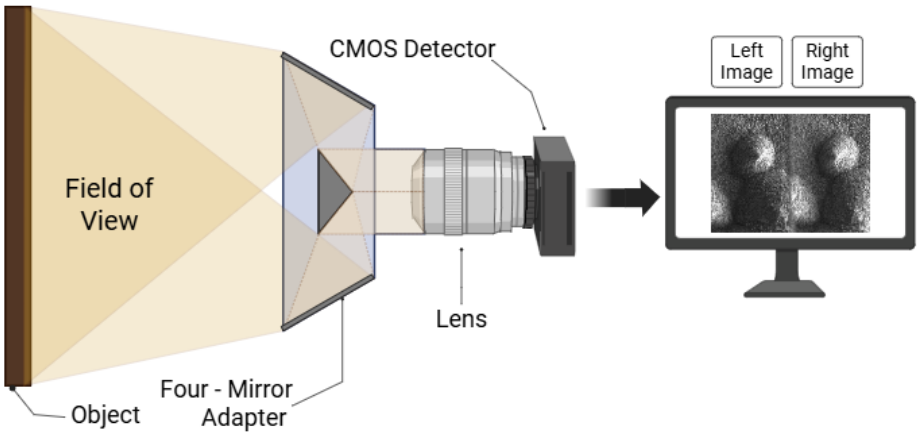

FIGURE 3.5: Schematic layout of the camera system, showing the optical path from the object plane through the lens system to the final image formation on the detector.

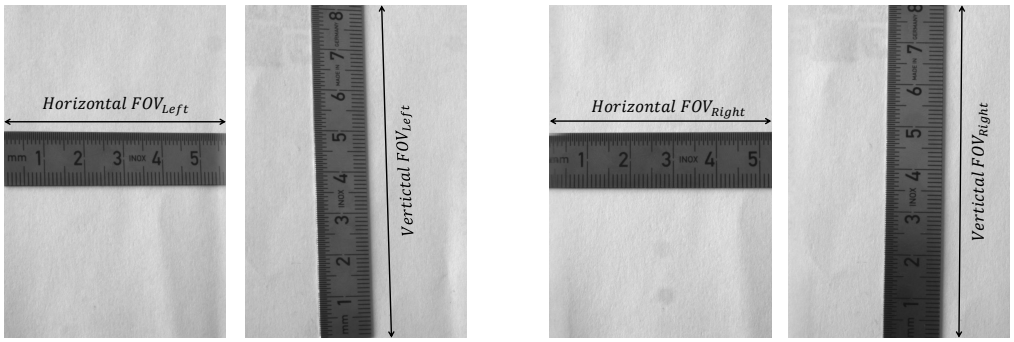

(A) Left camera (B) Right camera

FIGURE 3.6: Measured field of view for the left and right camera views, illustrating the horizontal and vertical spatial extent in object space.

3.3 Disparity Map

Following the implementation of the experimental setup and the feature extraction procedure described in section 2.3, the resulting depth map is computed to visualize the spatial relationships of objects in the observed scene, as shown in figure 3.7. Each pixel in the depth map represents the precise distance of the corresponding object point from the stereo camera system.

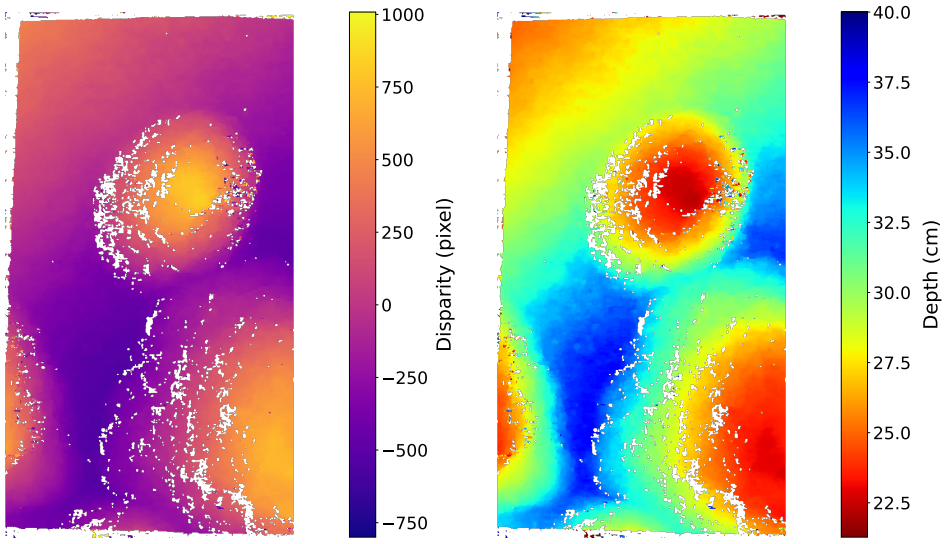

FIGURE 3.7: Disparity map (left) and corresponding depth map (right) for 3D reconstruction of the observed lunar regolith simulant pile shown in figure 2.4.

The construction of the depth map relies on the conversion of disparity values for each image point into depth measurements. This conversion is achieved through the utilization of calibrated camera parameters, as determined in section 2.2.2. These parameters include the tilt angle of the outer mirrors with the optical centre, baseline distance between the stereo camera pair, and focal length. The mathematical relationship between disparity and depth is articulated in equation 2.17, which governs the transformation process. The accuracy of the depth map is heavily dependent on the precision of the disparity map and the stereo camera's calibration.

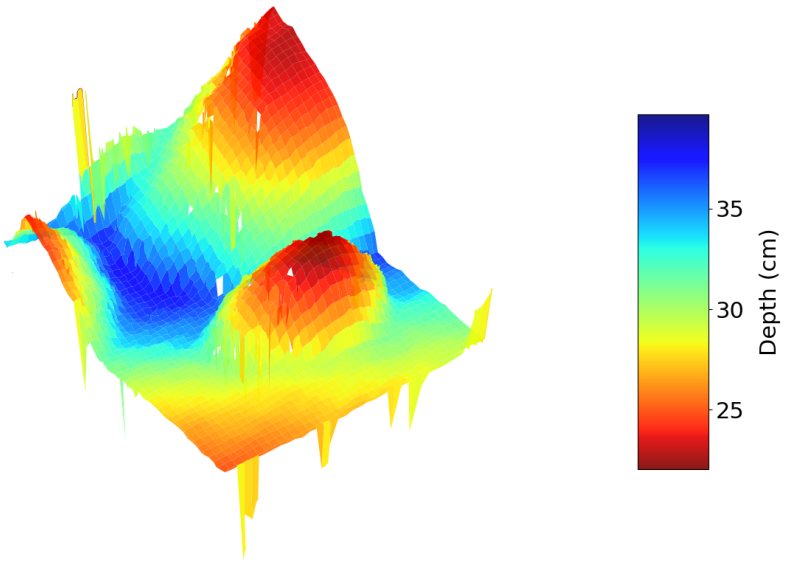

FIGURE 3.8: 3D surface reconstruction

Areas of low texture or featureless regions within the scene may yield less reliable disparity values, resulting in artifacts or discontinuities in the depth map. These limitations are addressed through interpolation techniques and smoothing algorithms, enhancing the overall coherence of the depth representation.

Leveraging the depth information, a 3D surface elevation model can be constructed, which interprets each depth value as an elevation point, effectively creating a detailed 3D surface as represented in figure 3.8. A clear visualisation of structural and spatial relationships can be rendered with the help of a smooth connected surface from the depth information of the object. Alternatively, the data can also be represented as 3D point cloud, depicting the specific location of each point in the world coordinate system. The point cloud distribution provides a detailed understanding of the relationship between the spatial positioning and depth of the object, with respect to its surroundings [3].

3.4 Experiments and Interpretation

3.4.1 Stereo Anaglyph Visualization

A stereo anaglyph offers another effective approach to stereoscopic visualization by combining stereo image pairs into a single, cohesive representation, specifically using red and blue colour channels. The input images undergo rectification to align them geometrically, ensuring accurate depth encoding. This technique involves superimposing the red and blue channels from the left and right rectified images, respectively, to encode depth information based on parallax between the two views [40]. When viewed through appropriately coloured glasses, this superimposition enables the viewer to perceive depth in the scene. The visual cortex of our brain processes the distinct colour inputs from both channels, resulting in a three-dimensional impression of the encoded scene [41].

Anaglyph techniques have been extensively applied in scientific contexts to enhance visualization of geological features and texture differences on planetary surfaces. For example, during NASA's Mars Exploration Rover Mission in 2003, such

methods were utilized to analyse terrain morphology and topographic variations [42]. Furthermore, the Perseverance and Curiosity rovers leverage advanced stereo camera systems to generate 3D visualizations, including anaglyphs, for examining rock textures, surface features, and overall environmental assessment. These visualizations not only aid scientific investigations but also support autonomous navigation on Martian terrain [3, 12].

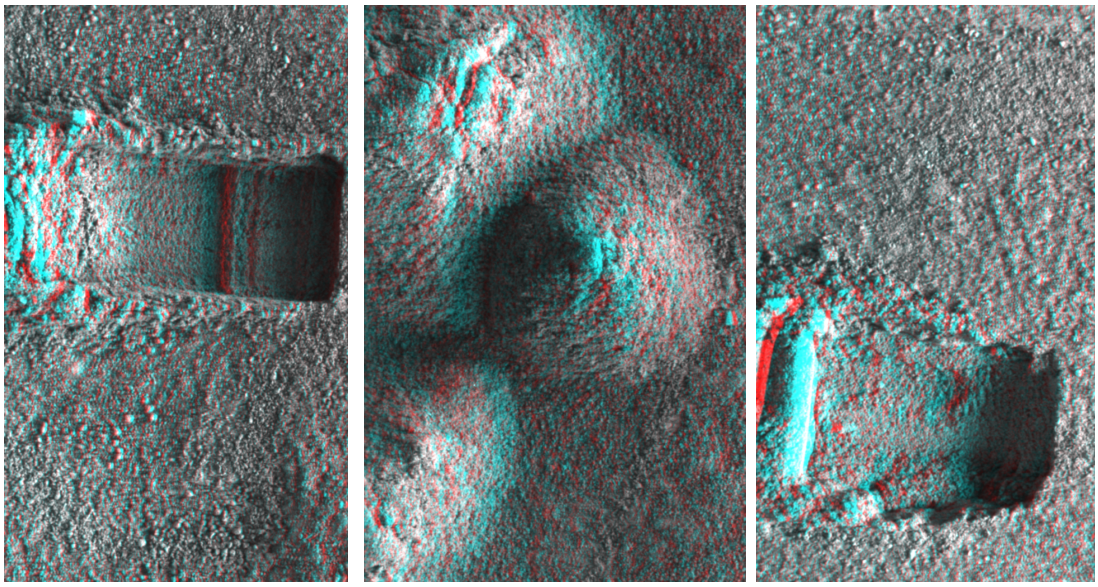

FIGURE 3.9: Stereo anaglyphs generated using calibrated stereo camera parameters and MATLAB stereo processing toolbox. Red and blue channels represents left and right camera views.

3D anaglyphs in figure 3.9 were created using the calibration parameters of the stereo camera. This process involved rectifying the images to align them properly and then superimposing them through MATLAB-based stereo processing toolbox [43]. The calibration parameters provided key information about the relative positions and orientations of the left and right cameras, as well as metrics to correct image distortion caused by the optics. Rectifying the images ensured they were aligned in the same coordinate system, which made it possible to generate accurate anaglyph images that maintain depth perception and spatial accuracy [3].

3.4.2 Angle of repose

Knowledge of the regolith properties is useful for design and planning of in situ resource utilization equipments, assistance in sample collection and storage as well as in preparation of the sampling site [44]. Geotechnical parameters of regolith such as shear strength, cohesion, bearing capacity, and angle of repose is considered vital for the development of lunar infrastructure. The stability of features like craters and hills on the lunar surface can be inferred with an important characteristic called angle of repose of the surface material. The steepest angle formed by a pile of aggregate before experiencing failure is defined as an angle of repose [45]. In planetary science, it is an excellent proxy for particle size, regolith flowability and cohesion of regolith [46]. These properties of the lunar regolith is highly affected by particle size, as the attractive forces from intermolecular and interatomic surface interaction of particles become a dominant factor [47].

To better understand how the angle of repose of lunar regolith is influenced by these factors, the stereo camera will help to study it with higher accuracy. Combining it with other geophysical properties, a better understanding of the close range study site can be obtained. The European Astronaut Centre lunar regolith simulant 1 (EAC-1A) is utilised for this experiment. With a comparable chemical composition with the Apollo 17 samples, the EAC-1A samples contains 43.7% of SiO_2, 11.9% MgO, 4.2% $(Na_2O + K_2O)$ and 2.4% TiO_2 [29, 48].

The fixed funnel method of measuring static angle of repose was employed, where a base plate diameter of 37 mm, and a fixed funnel at the height of 50 mm from the plate is used to gradually pile up the simulant onto the plate. Acquiring a stereo image pair of the regolith simulant pile in two different perspectives, helps us to validate the accuracy of the calculated angle of repose geometrically 3.10a, with the one obtained from the cross-section of the 3D reconstructed image of the target as shown in figure 3.10b. This also helps us to evaluate the measurement accuracy of the stereo image processing.

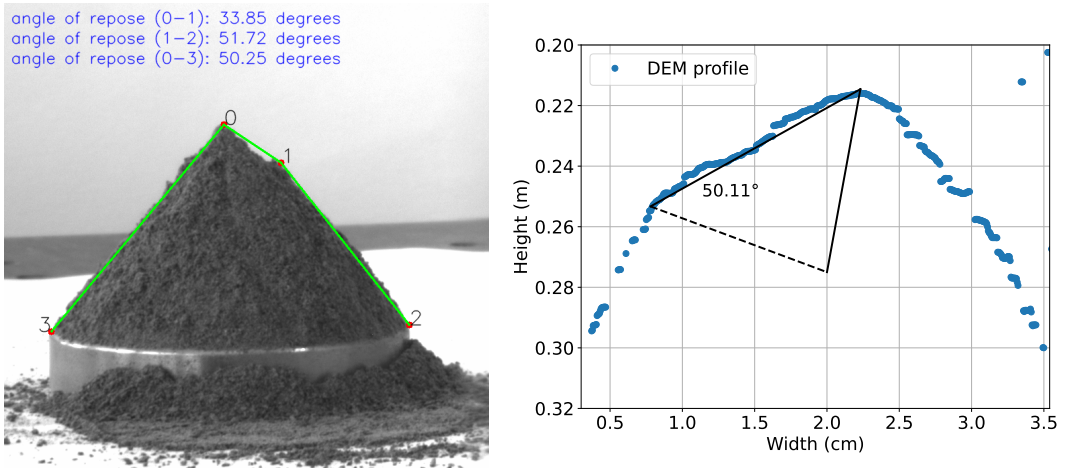

(A) Geometrically calculated angle of repose with respect to base plate using front view images of the dust pile

(B) Angle of repose with respect to base plate, extracted from profile of the 3D image

FIGURE 3.10: Static angle of repose of for regolith simulant EAC-1A, extracted via stereo camera

Upon comparing the two resulting angle of repose values, as shown in figure 3.10, the value extracted from the 3D image profile of about 50.11° with respect to the base plate, agrees well with the geometric calculated value of angle of repose of 50.25° for the regolith simulant. Additional information is also obtained from top of the dust pile, where a secondary angle of repose (denoted by angle between the points 0 and 1 in figure 3.10a) of about 33.85° is observed, pointing towards the cohesive properties of the material used.

The range of particle size in EAC-1A is 0.02 µm - 2000 µm, with lower weight percentage of the finer particles (1 µm - 0.02 µm) without any significant sphericity [29]. Due to its irregular particle shape, EAC-1A showcase a higher cohesive behaviour, resulting in increased slope stability with little compaction. As pointed out by Easter [46] in their study regarding the relation of particle size distribution and the angle of repose of the lunar regolith simulant, finer particles have a significant effect on the angle of repose of the sample. This is clearly observed in the experiment results discussed in this section.

To further analyse and perform a comparative study on the effects of particle size distribution on the angle of repose of regolith simulant, NU-LHT-2M lunar highlands regolith simulant was used for testing [49]. This simulant sample is based on the chemical composition of samples from Apollo 16's landing site, containing 46.3% of SiO_2, 24.7% Al_2O_3, 5% FeO, 6.8% MgO and 0.10% TiO_2 [50]. A similar procedure was used to measure the angle of repose of the simulant pile. However, due to the presence of much finer particles, the stereo processing algorithm was not able to successfully reconstruct a 3D image of the sample. Such result is expected as the NU-LHT-2M simulant contains particles not greater than 1 mm in size, which is out of the range of depth resolution of the camera.

3.4.3 Albedo Measurement

A photoclinometric approach is usually employed for surface reconstruction of planetary bodies. Techniques such as SfS (Shape from Shading) or SAfS (Shape and Albedo from Shading) can generate pixel-level digital elevation models (DEMs) of the planetary surface with high spatial resolution [51]. The quantized measurement registered at an imaging device is the irradiance values corresponding to the object radiance for a specific surface orientation and surface material property. Often depicted as gray levels in an image, the surface properties can be inferred by detail analysis of this information. With more than one view of the scene and varying illumination conditions, surface shape and albedo can be computed, with surface photometry, along with the orientation of the light source and viewing angle of the camera [52]. Such a photometric stereo method generates high quality pixel-level surface elevation products for planetary surface reconstruction applications [53]. Unlike the traditional photometric stereo method as introduced by Woodham [54] in 1980, more advanced methods have been introduced in Yutu-2 rover stereo imaging, for lunar topographic mapping applications, which involves an integrated lunar reflectance models and a physical sensor models [53]. This method can generate high-resolution topographic reconstruction with the help of ground-based images, acquired with a varying illumination environments. The advantage of using a monocular stereo camera for such application is the ability to capture the scene with the same viewing condition, but with two different perspectives. This further helps in extracting the photometric differences between the stereo pair, simplifying the image processing algorithm. The narrow FOV, and higher spatial resolution of the proposed camera, will effectively create a stereo image pair as an input for such techniques.

Photometric stereo processing relies on several critical assumptions to simplify the computation and make the method more manageable. First, it assumes that the imaged surface exhibits Lambertian reflectance. This means that the intensity of the reflected light depends solely on the incident light's angle and the surface normal, disregarding any specular reflections [3]. Additionally, the light source is considered to be a point source located at an infinite distance, which implies that the rays striking the surface are parallel. Atmospheric scattering is also ignored, and because the images are captured within a short time span (approximately within ten minutes), the sun's altitude angle is assumed to be constant.

Although a minimum of three images is sufficient for computing the surface properties using this method, at least six images are typically captured to ensure redundancy and guarantee that nearly every region of the scene is illuminated at least once. The experimental process is executed in several steps:

1. *Image Acquisition*: Multiple images are taken from a fixed camera position while varying the illumination direction. This multi-view setup is crucial for capturing different lighting conditions across the surface.

2. *Light Source Position Calculation*: The direction of the light source is determined by calculating its position in a Cartesian reference frame. This computation is based on the time of the image acquisition and the known location of the camera relative to the sun's azimuth and altitude angles.

3. *Processing Pipeline*: The computed light direction information, along with the multi-illuminated images, is fed into the photometric stereo processing pipeline. Using the relationship in equation 3.1

$$I(x, y) = \rho_(x, y)(L.N_(x, y)) \tag{3.1}$$

   where $I(x, y)$ is the intensity at each pixel, $\rho(x, y)$ is the surface albedo, $L = (L_x, L_y, L_z)$ is the light direction vector relative to the camera, and $N_(x, y)$ is the surface normal at that point, the system extracts both the surface normal and the reflectance albedo.

To evaluate how illumination source geometry and the effects of shadowed regions to the results, experiments were conducted on three different types of regolith analogue surface features: a relatively flat surface with little to no shadowing (3.11a), a piled material surface with uplifted features that create shadows (3.11b), and a surface with depressions that cast shadows on the crests (3.11c).

The resulting relative albedo maps shown in figure 3.11, indicate that well-lit regions tend to have uniform albedo values, as expected for a test surface made of the same regolith analogue material. However, the resulting maps also reveal inconsistent results in heavily shadowed areas and for pixels with specular reflections. These issues suggest that incorporating additional images with varying lighting geometries and obtaining precise light source data could yield more robust and accurate surface reconstructions [3].

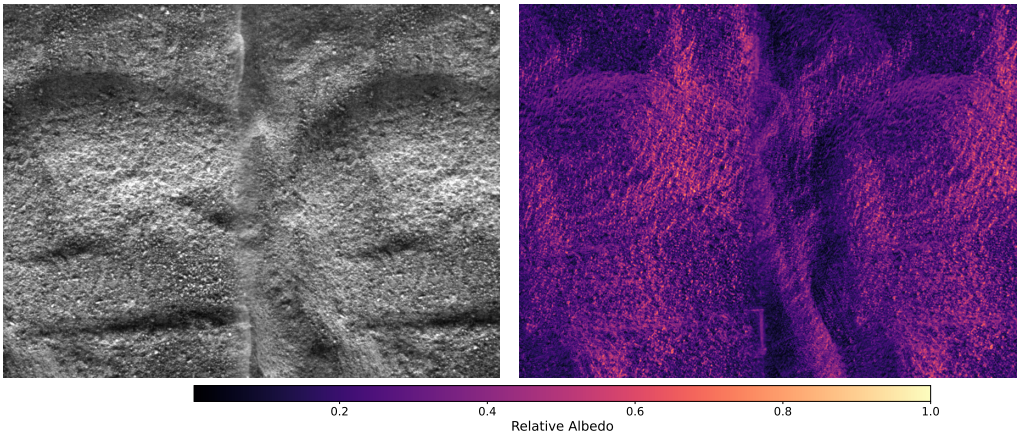

(A) Relatively flat surface

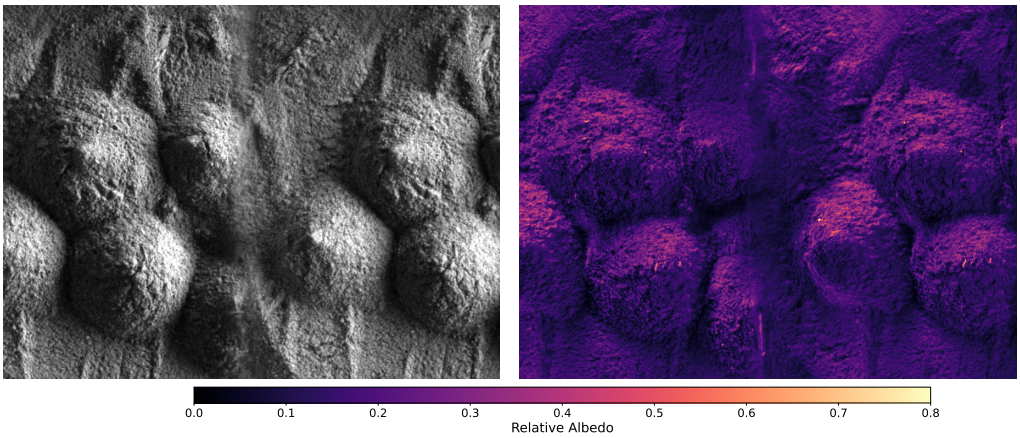

(B) Dust pile

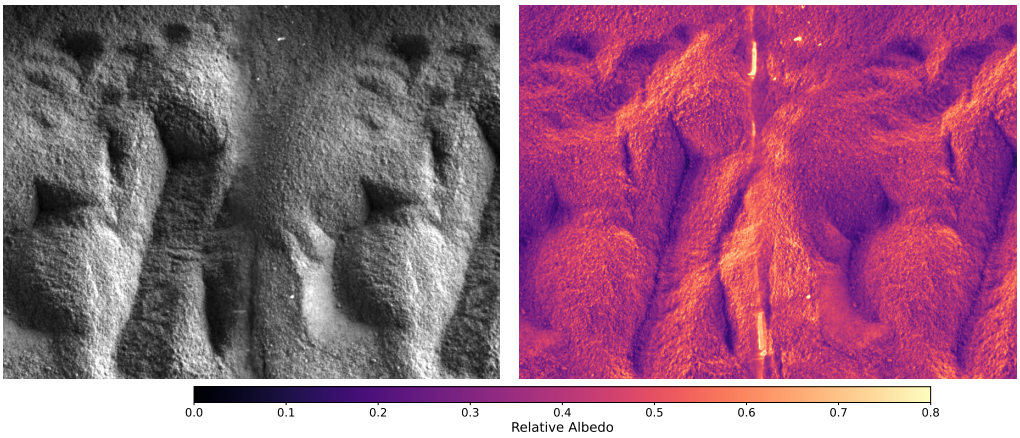

(C) Surface with mild features

FIGURE 3.11: Relative albedo extracted with varying illumination based photometric stereo method

3.5 Performance Quantification

3.5.1 Shape Measurement

The accuracy of the 3D reconstructed profile of an object necessitates rigorous verification. For this purpose, a cylindrical rod with a diameter of 37 mm, covered with a random speckle pattern, was utilised as a target object shown in figure 3.12. The speckle pattern comprised dots with sizes ranging from 1 to 2 mm. A well-illuminated image of the decorated rod was captured and subsequently processed using the stereo reconstruction pipeline. This facilitated the morphological analysis of the curved surface with predefined dimensions and enabled the reconstruction of the profile to assess measurement accuracy. By geometrically fitting the extracted profile obtained from the depth map, the diameter of the cylindrical rod was estimated. A comparison between the reference dimensions and the calculated values provided an estimation of the relative error in the measurement results.

As illustrated in figure 3.13, a 3D surface representation of the cylindrical rod was successfully reconstructed, demonstrating a height variation of approximately 1.54 mm per millimetre of horizontal displacement. These findings validate the efficacy of the employed 3D shape reconstruction methodology utilizing a stereo camera system.

FIGURE 3.12: Cylindrical rod with speckle pattern used as a target to extract 3D reconstruction accuracy

For shape measurement context, a quadratic curve fitting method was implemented to retrieve a 2D profile of the object. The shape profile along the line OP extracted from the depth map, along with the fitted profile is presented in figure 3.13b. The measurement results are in good agreement to the actual dimensions of the rod, depicting an accuracy better than the required 1 mm depth resolution, with a mean error of 423.2 µm relative to the reference values. The radius of the cylinder can be computed quantitively with the approach mentioned in Luo and Chen's study [55] of measuring deformation of curved surface using a stereo vision system, where the equation of the cylindrical surface is solved, determining both the position of cylinder's centreline and the radius of the test object with the help of the camera's intrinsic and extrinsic parameters.

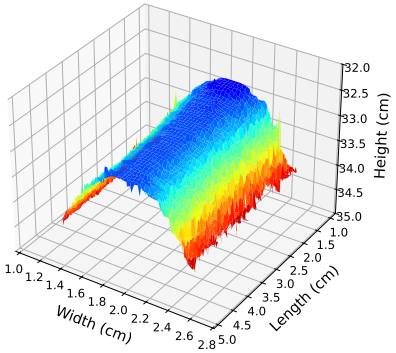

(A) Reconstructed profile of the cylinder surface

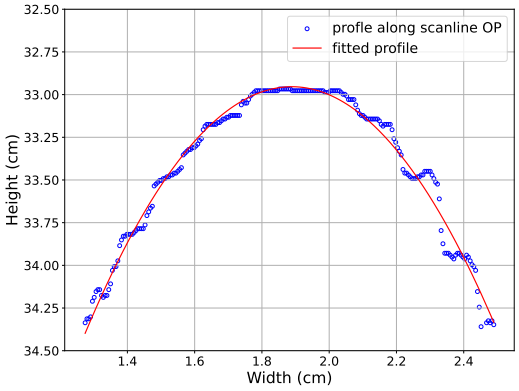

(B) Cross-section profile of the cylindrical surface reconstruction, illustrating the height variation across the surface.

FIGURE 3.13: Reconstructed 3D profile of the cylindrical surface, showing the spatial distribution of height measurements.

3.5.2 Resolution Test

The resolution of an optical system quantifies its ability to resolve the finest details in an image and faithfully reproduce them. Several factors, including sensor pixel size, illumination conditions, and the optical configuration, play critical roles in determining the resolution of an imaging system [3]. Resolution is commonly expressed in terms of line pairs per millimetre (lp/mm) combined with the contrast reproducing capability of the lens system. It can be defined as the ability of the system to resolve an image of a line pair consisting of alternating black and white squares at a specific contrast reproduction capability.

The limiting resolution of a camera is governed by the Nyquist criterion and can be calculated as [56]:

$$\text{Nyquist Limit}[\frac{lp}{mm}] = (2.P_s.1000)^{-1}$$

where P_s represents the pixel size of the sensor in millimetres. This limiting resolution corresponds to the resolution in the image space (ξ_{image}). By scaling the limiting resolution with the system magnification factor (m) as described in equation 2.5, the resolution in the object space (ξ_{object}) can be determined. The Nyquist limit for the camera was determined as 144.9 lp/mm, and the object space resolution is 9.135 lp/mm, translating to a spatial resolution of 54 µm per pixel. The results effectively exceeds the minimum requirement of 150 µm per pixel spatial resolution.

The contrast limitation of a lens system is a critical factor in determining its resolution. It is essential to recognize that resolution cannot be meaningfully defined without reference to a specific contrast level, as the perceived sharpness and clarity of an image depends on the system's capacity to distinguish fine details against their background. The actual resolving power of the imaging system is governed by its ability to dissolve the space between adjacent details and preserve sufficient contrast between closely spaced structures. In practice, even when the sensor or imaging medium possesses a high pixel density, the system may still fail to resolve individual features if the contrast between them is too low. In such cases, adjacent details may appear visually merged or indistinct, thereby limiting the effective resolution of the system [3].

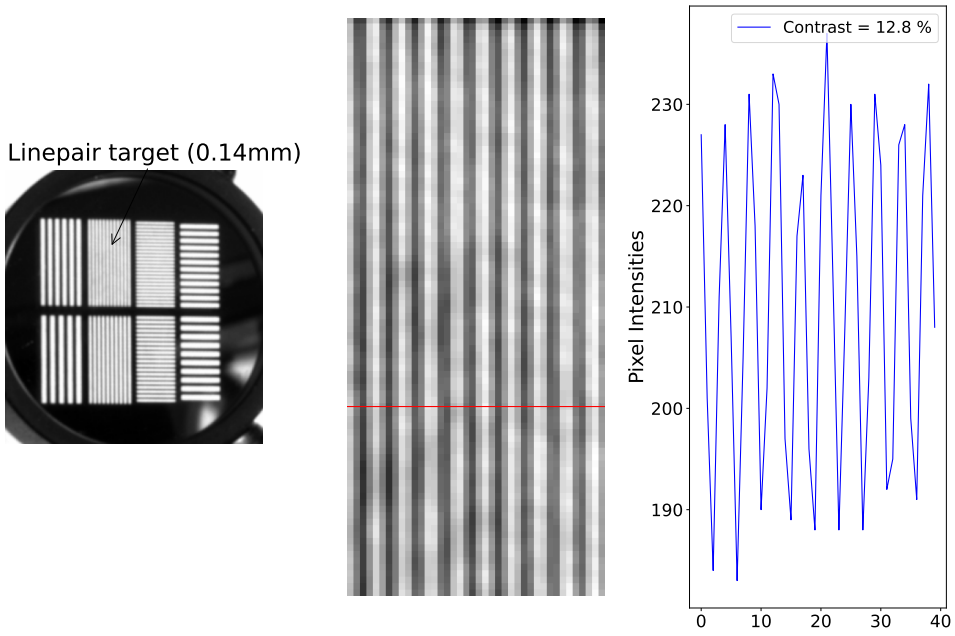

FIGURE 3.14: Resolving power of the camera system determined using a 0.14 mm line-pair resolution target (left). The pixel intensity plot (right) is derived from the cross-section (red line) of enlarged target image (middle).

To visually assess the image resolution achieved by the proposed camera system, a straightforward resolution test was conducted using Ronchi ruling targets as shown in figure 3.14. These targets feature periodic square wave patterns consisting of alternating dark and light lines, with spatial frequencies ranging from 1.5 to 3.57 line pairs per millimetre (lp/mm), where one line pair is defined as a single dark and light line. Such targets are particularly well-suited for evaluating the object space resolution of optical systems due to their uniform and high-contrast structure, which allows for a clear determination of the system's ability to resolve fine spatial details. In this test, the finest pattern, characterized by a bar interval of 0.14 mm, was selected for detailed analysis. The contrast of the resulting image was quantitatively evaluated by measuring the pixel intensity values across the pattern, providing a direct assessment of the system's contrast transfer capabilities at the highest tested spatial frequency. The analysis revealed that the system is capable of resolving up to 3.57 lp/mm in image space. When converted to spatial resolution in object space, this corresponds to an effective pixel pitch of 56.69 µm per pixel, assuming a known magnification factor of 0.063. This resolution was achieved at a contrast level of 12.8%, which is a meaningful indicator of the system's performance under real-world imaging conditions. The results demonstrate that the camera system is capable of resolving fine spatial details with acceptable contrast, thereby validating its suitability for applications requiring moderate to high-resolution imaging [3].

The resolution of an optical system is determined by multiple factors, which include blur caused by diffraction, optical aberrations, the spatial distribution of object details, and the sensor's ability to detect contrast at various levels of detail. Among these, diffraction-induced blur and aberrations induced from imperfections in the lens design significantly impact the final image quality. Equally important is the sensor's contrast detection capability, which governs how well details of a specific size can be captured. Modulation Transfer Function (MTF) testing is widely regarded as the most reliable method for evaluating the resolution of an optical system. Specifically,

MTF50 testing, often referred to as Spatial Frequency Response (SFR), plays a critical role in this process. It not only quantifies resolution across varying levels of contrast but also provides valuable insights into system misalignments, enabling comprehensive analysis of the system's performance [57].

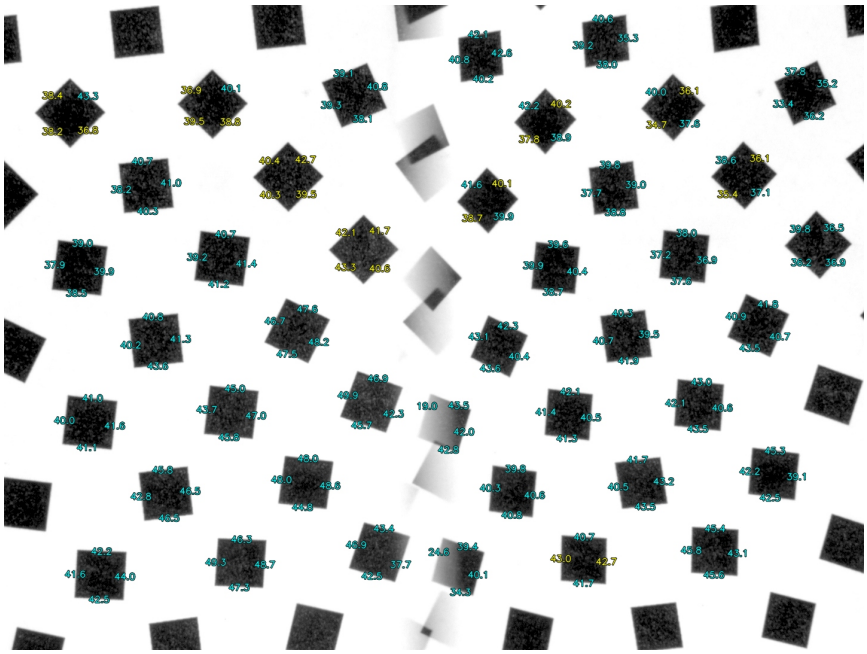

FIGURE 3.15: Test grid used for the slanted edge method to compute MTF frequencies, with annotated values on the corresponding rectangle edges.

To accurately evaluate the acuity of the camera system, the MTF50 values are computed at the edges of geometrical shapes, particularly rectangles, using the slanted-edge method. This method is specifically developed to handle images that exhibit considerable lens distortion [58]. For testing purposes, a grid of rectangles is utilized as the test chart as shown in figure 3.15. These rectangles are arranged in a regular pattern at fixed intervals. The test chart is imaged at varying distances ranging from 150 mm to 400 mm from the camera. The open-source tool MTF Mapper is employed to record spatial frequency data, specifically MTF50 values, at both the centre and corners of the image plane for each camera view [59]. By implementing performance measurements using a translating target relative to the camera, this method allows for determining the most effective position of an object to achieve maximum sharpness in captured images.

The results, as presented in figure 3.16, indicate that the resolution requirements of the camera aligns well with the derived working distance. Each rectangle within the test chart is annotated with specific values that facilitate the assessment of sharpness across different regions of the image plane.

Spatial Frequency	**Simulated Setup**	**Actual Setup**
MTF50 (lp/mm)	56	45.5

TABLE 3.2: Performance comparison between simulated and experimental camera setup

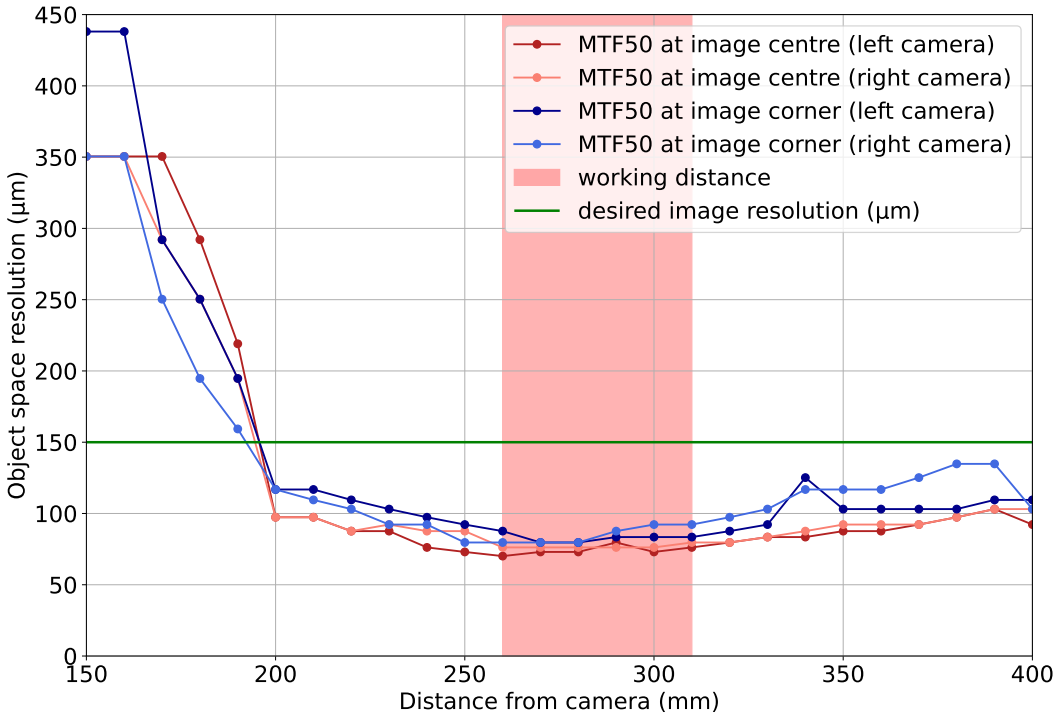

FIGURE 3.16: The MTF-50 curve, expressed in object space resolution as a function of increasing distance from the camera, is shown for both the centre and the corner of the image. The test chart displayed in figure 3.15 was used for the MTF50 computation.

Figure 3.16 shows the MTF50 curve with varying working distance. The peak values of the curve corresponds to the range of position of object with best focus position and sharpness in the captured images. The red overlay region indicates the working distance of the camera calculated in equations 2.13, 2.14. This shows that the camera is able to image objects within the viewing range of the camera, with acceptable resolution of MTF >0.5 at Nyquist frequency of 144.9 lp/mm. The optimal object space resolution observed with this resolution test setup lies in the range of 70 µm to 72 µm per pixel within the region of effective working distance, successfully exceeding the desired spatial resolution requirement for the camera.

Additionally, figure 3.17 delves deeper into the analysis by depicting the MTF50 values across the image plane, divided into meridional and sagittal plots. These visualizations effectively reveal distinct performance characteristics in each direction. The sharpness values extracted from edges oriented along radial lines and tangential edges relative to the centre circle of the image are computed as sagittal MTF50 and meridional MTF50, respectively. This analysis is particularly significant for the overlapping region of the FOV between the left and right cameras, as highlighted by the prominent edge visible at the centre of the image. In contrast to conventional cameras, which rely solely on lens curvature to direct light onto the imaging plane and often exhibit sharpness values concentrated at the image centre with a gradual decrease radially outward, this system demonstrates more consistent sharpness across the entire imaging plane.

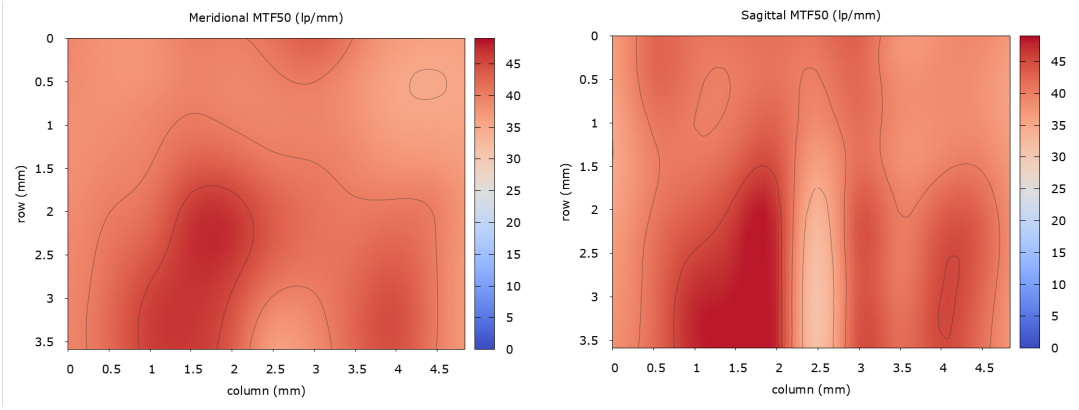

FIGURE 3.17: Plots of MTF50 values across imaging plane, as a function of distance from the centre of the lens, for both the meridional (left) and sagittal directions (right). The colorbar indicates MTF50 values, while plot rows and columns correspond to actual detector dimensions.

Chapter 4

Discussion

Like any engineering and scientific system, prototype design can not be developed without any limitations. Several factors affecting the accuracy and reliability of stereo imaging results must undergo critical evaluation to reveal its effective performance. This chapter elaborates on a comprehensive discussion on the limitations of the camera, and identifies these factors in order to propose further analysis and refinement required post prototyping phase. Understanding the limiting constraints of the system becomes essential to assess its readiness for real mission scenarios, and provide insights into current performance boundaries. In addition, an outline of future work in terms of potential design enhancements and extended experimental proposal is presented to expand the scientific and operational capabilities of the stereo imaging system.

4.1 Limitations

Designing the stereo camera involved balancing several competing factors. To capture a scene in high resolution, the camera system needs the optical axes of the two cameras to converge sufficiently so that both cameras overlap on the object of interest, which is crucial for accurate stereo matching. However, this increased convergence can limit the wide field of view needed for navigation, especially on landers where a broader view of the environment is important. Additionally, the camera's fixed focal length and aperture restrict its depth of field. This limitation makes it difficult to capture distant objects with acceptable sharpness or to focus precisely on targets at varying distances. The initial setup, specifically, the positioning and cant angle of the cameras relative to the lander, plays a critical role in determining key parameters such as working distance, FOV, focal length, and baseline length. These specifications are essential for producing high-quality images and for effective stereo image processing. Further, the design was constrained by the available optical components. The limitations in off-the-shelf products, market costs, and the inability to customize components meant that our choices were limited. This, in turn, affected the achievable spatial resolution and the overall accuracy of the stereo imaging process [3].

The dimensions of the mirrors and the reflective prism, serving as the inner and outer mirrors respectively, were computed using a comprehensive geometrical approach. The height and width of the outer mirrors must precisely align with the prism's dimensions so that, when assembled, the path of the light rays is obstructed by any component. This ensures that the entire set of light rays reflected from the outer mirrors is efficiently directed onto the inner mirrors, thereby maximizing the FOV captured at the detector [22]. In addition, the material properties of the mirror surfaces play a crucial role in effectively reflecting and directing the light for optimal imaging performance.

The placement of these reflective components, which is partly determined through analytical calculations and further refined via geometric optimization, poses significant

challenges in maintaining the camera system within the prescribed size and weight requirements. These factors underscore the complex trade-off inherent in designing a stereo camera system. Balancing image quality, FOV, and practical design constraints ultimately shapes the final performance and functionality of the stereo imaging system [3].

The spatial distribution of the Modulation Transfer Function (MTF) across the image plane as illustrated in figure 3.17, the MTF50 values exhibit a noticeable concentration in the lower region of the imaging plane, particularly towards the central area of the detector. This non-uniform distribution suggests a deviation from ideal optical performance and highlights a potential misalignment between the reflective prism and the detector plane. The observed MTF50 contours indicate that the image formation is not occurring precisely at the intended image plane along the optical axis. Instead, the image may be forming either in front of or behind the detector, which results in a degradation of image sharpness and resolution in certain regions of the FOV. This misalignment may arise from a combination of factors, including manufacturing tolerances in the prism assembly, mechanical inaccuracies in the detector mounting, or limitations in the optical design that do not fully account for the angular deviations inherent in stereo imaging configurations. As a result, the system may struggle to maintain consistent feature matching and depth accuracy across the entire image, especially in areas where the MTF is lowest. Experimental validation through iterative alignment and MTF measurement will be essential in achieving a more uniform and optimal image quality across the entire field of view [3].

Currently, the system employs a monochrome CMOS sensor, which is limited in its ability to capture a broad range of the light spectrum, as it is not sensitive to wavelengths outside of the visible range (400 nm–700 nm). This constraint means that imaging in only greyscale results in the loss of chromatic variations and additional spectral information, which could be critical for surface analysis. Replacing the current detector with a colour sensor that supports three or more channels would enhance the information gathered from the scene and provide further insights into surface properties [60]. Additionally, because the optical design incorporates a coupled set of square mirrors as the first surface of the lens system, only cropping is observed as a geometric aberration rather than vignetting. Vignetting typically occurs when the lens format is smaller than the detector format, whereas cropping happens when the lens format is larger than the detector format [61]. Nevertheless, since only half of the detector receives the image of the virtual camera, a subtle interference line appears at the centre of the detector, where there is an overlap between the left and right images, resulting in a blurry region. This overlapped region consists of detector pixels that do not contribute meaningful information to the final image.

Beyond the limitations imposed by the optical design and camera configuration, the stereo image processing also encounters several bottlenecks, particularly when applied to single-detector stereo imaging. The initial step in the processing pipeline is the rectification of the stereo pair [3]. Unlike conventional stereo imaging systems, which rely on pre-calculated camera intrinsic and extrinsic parameters obtained through calibration, the proposed stereo system utilizes an uncalibrated stereo rectification method. This feature-based algorithm is generally employed for systems with non-parallel optical axes, making it heavily dependent on epipolar geometry and the availability of distinct features within the scene. Although the optical setup in this system exhibits minimal distortion, enabling effective computation of the fundamental matrix for image rectification, a more robust approach would involve estimating the distortion coefficients for each camera separately. Subsequently, the images could be corrected using the resulting calibration camera matrices to further enhance the

stereo matching process.

4.1.1 Factors Contributing to Stereo Matching Inaccuracies

Further inaccuracies in depth estimation and 3D reconstruction is provided by following source of errors during stereo matching process:

1. *Camera calibration errors:* Discrepancies introduced in geometric transformation due to calibration errors, arising from imprecise measurements. These inaccuracies ultimately lead to errors in the computed epipolar lines and, consequently, in the matching of corresponding points [3].

2. *Poor image resolution:* The spatial resolution of the captured images directly impacts the stereo matching process. Low-resolution images reduce the amount of detail available for feature detection, thereby complicating the accurate identification of corresponding points between the stereo pair. This degradation in feature quality results in coarser depth estimation results, particularly for scenes with fine structural details.

3. *Low-contrast images:* Contrast is a critical factor for distinguishing features within an image. Low-contrast conditions, which may result from improper illumination, overexposure, or surface properties of the object, compromise the ability of matching algorithms to detect reliable features. Consequently, low-contrast images can lead to ambiguous or incorrect feature correspondences, and ultimately, to inaccurate stereo matching. Additional contrast enhancement method can help remove such errors [3].

4. *Limited view overlap:* For successful stereo matching, there must be a significant overlap between the FOV of the two virtual cameras. Insufficient view overlap restricts the common region, visible in stereo pairs, available for feature matching, reducing the number of corresponding points and increasing the likelihood of feature mismatching. This limitation further add to the challenges of generating accurate disparity maps.

5. *Lighting conditions:* Variations in lighting conditions such as shadows, glare, or uneven illumination, can alter the appearance of objects between the two images. These variations can hinder the consistency of detected features and distort the appearance of texture, making it difficult for matching algorithms to correctly identify corresponding points [3].

6. *Low textured object:* Objects with low texture or minimal variation in surface patterns present a notable challenge during stereo matching. Without sufficient textural information, traditional matching algorithms struggle to confidently identify and align features between the stereo images. This lack of distinguishable features often results in incorrect or sparse correspondences, thereby affecting the robustness and accuracy of the depth estimation process [3].

7. *Position of mirrors (rotation or misalignment):* In optical systems that incorporate mirrors, even minor inaccuracies in the placement or orientation of these mirrors can lead to rotational errors or misalignment in the captured images. Even slight deviations from the optimal configuration may result in significant projection distortions, thereby generating false correspondences of epipolar lines and causing errors when determining corresponding points in the stereo image pair. Since epipolar geometry requires that corresponding object points be

aligned along the same scanline, any misalignment of the mirrors produces vertical parallax if the mirrors are not maintained parallel to the planes perpendicular to the respective camera's optical axis.

Addressing such misalignments is particularly challenging, as the successful operation of the stereo processing pipeline depends on aligning the mirrors with a minimal toe-in angle to reduce vertical disparity between the stereo pairs. Stereo matching algorithms are generally designed with the assumption that the vertical disparity is no larger than one pixel; exceeding this threshold introduces additional complexity in reliably identifying corresponding features between images.

Designing a camera system, particularly for lunar lander application, dust mitigation becomes significant, especially when operating in close range from the lunar surface. The lunar regolith with fine dust particles are known to interrupt the imaging capabilities of cameras, while posing serious challenges on its ability to view scenes clearly. Known for their electrostatic properties and abrasive nature, these particles can accumulate on optical components, leading to a gradual decline in imaging performance [62, 63]. No protective component is taken into consideration at this initial stage of development of the proposed camera design. The first optical surface are fully exposed to surrounding dusty environment, allowing contact between dust particle with the optical components. Accumulation dust particles on camera, especially over mirrors can heavily introduce stray light interference with the light entering into the system, degrading the image contrast. With increasing dust build-up, the camera performance keeps deteriorating. A simple solution would be to use a removable protective cover for the camera and use it as a shield for dust exposure when the camera is not operational, slowing down the performance degradation process, ensuring image quality is maintained for extended durations. Additional mitigation techniques could be integrated in the design, such as mechanical shutters, self-cleaning coatings, to provide further protection and reliability of observations.

Achieving microscopic resolution in stereo imaging necessitated a design trade-off, leading to the selection of a fixed-focus lens. This approach eliminates the need for a refocusing mechanism, reducing mechanical complexity and ensured a high resolution imaging results without requiring manual adjustments. This decision ensured consistent imaging quality, especially operating in close-range imaging tasks. Additional moving components introduce alignment errors, increased calibration needs, and increases bulkiness of the system. For future implementation, this characteristic can be traded off based on the mission objectives and operational constraints of the camera. The ability to adjust focus could provide a greater flexibility of imaging close and far range target objects, and also be beneficial for multi purpose operations like surface mapping and surface characterisation tasks allowing the camera to perform both microscopic and wide-field imaging without sacrificing resolution, making it more versatile.

4.2 Extended Analysis and Experimental Proposals

The exploration of lunar regolith through advanced imaging and analysis techniques offers profound insights into its physical and compositional characteristics. High-resolution depth information, when effectively integrated into scientific studies, has the potential to reveal intricate details about the lunar surface, furthering our understanding of its evolution and behaviour. This section discusses the properties that

could be inferred from such data, as well as the broader applications of advanced imaging technologies in the study of the lunar regolith.

High resolution lander imaging systems can also serve as a surveyor or auditor for sample collection activities. By combining depth information with high-resolution imaging, precise location of regions of interest can be assessed, improving the efficiency and scientific value of sample-return missions. Moreover, the use of a monochrome detector with colour imaging capabilities adds versatility to the approach. By employing band-pass filters or post-processing techniques, it becomes possible to extract spectral information that reveals compositional diversity [60], further enhancing the scientific utility of such imaging system [3].

The photometric parameters of the lunar surface derived from a high-resolution stereo camera, such as albedo, bidirectional reflectance distribution functions (BRDF), and topographical features, provide essential ground truth data for radiative transfer modelling of lunar remote-sensing data [64]. These parameters quantitatively describe how the lunar surface reflects, absorbs, and scatters incident sunlight. By accurately measuring these properties in situ using stereo imaging, reliable baseline values can be established against which the radiative transfer models used to interpret orbital observations are calibrated [7].

Radiative transfer models simulate the complex interaction between solar radiation and the regolith, including effects such as multiple scattering, absorption by surface materials, and thermal emission. When these models are constrained with ground truth photometric data, the resulting simulations more accurately represent the lunar surface's physical and compositional characteristics [64,65]. This improved accuracy is critical because it enhances the interpretation of remote-sensing images, such as those provided by instruments aboard lunar orbiters, and leads to a better understanding of key parameters like surface composition, roughness, and thermal inertia [3,66].

An interesting extension of the current imaging capabilities would be to acquire panchromatic imaging at night. By integrating an LED illumination setup similar to the setup of MasCam camera on board the MASCOT mission, the system can actively illuminate the lunar surface, especially when ambient light is unavailable [67]. In this approach, LED arrays emitting at specific wavelengths, 470 nm (blue), 530 nm (green), 640 nm (red), and 805 nm (NIR), cab be employed to sequentially light up the target area with monochromatic light. Individual images captured under each wavelength are then digitally merged to form a comprehensive panchromatic image.

This methods poses several advantages over conventional imaging conditions. First, active illumination ensures that high-resolution images can be obtained regardless of the solar cycle or natural light conditions, which is particularly important for night-time imaging. Second, by using different spectral bands, the process enhances the detection of subtle surface features and material variations that might be invisible under broad-spectrum or low-light conditions. This multispectral illumination also improves image contrast and resolution, allowing for more accurate assessments of the lunar surface properties. Such detailed imagery can be critical for refining photometric models, supporting the radiative transfer analysis of orbital remote-sensing data, and ultimately providing ground truth for calibrating these models [3].

4.2.1 Soil Mechanics Experiment

Soil mechanics experiments aimed at understanding wheel-soil interaction are essential for ensuring the efficiency and reliability of robotic exploration on lunar terrain. Lunar regolith, with its unique geo-mechanical properties, poses specific challenges

for mobility systems, making it vital to analyse parameters such as particle size distribution, density, porosity, cohesion, adhesion, and the angle of internal friction [68]. These properties have been extensively studied through manned lunar missions, autonomous expeditions, and laboratory experiments using lunar soil samples returned to Earth [3, 69].

High resolution 3D reconstruction employs detailed visualisation of these interactions. By simulating these interaction, detailed insights can be extracted about surrounding soil deformation, and help investigate the sinkage, load-bearing capacity and traction performance of the regolith under the wheels. Previously performed experiments by Viking Lander's trench-digging, and the Sojourner rover's wheel dynamics observations, established relationship between soil parameters like soil cohesion, friction angles from captured the behaviour of soil-wheel interaction. The patterns of soil compaction, particle displacement, sinkage depth and steepness of imprint wall, can be visualised to enable estimation of critical parameters of lunar regolith [68]. Such experiments are performed based on terramechanics theory, improving the prediction of wheel slippage, energy consumption, and terrain traversability, ultimately enhancing robotic exploration capabilities. By observing soil imprints created during experiments, researchers can assess porosity, density variations, and shear behaviour. This non-invasive technique eliminates the need for physical soil sampling, making it invaluable for extraterrestrial missions where resources and mobility are limited [3, 70].

4.2.2 Regolith Characterisation

A comprehensive lunar regolith characterisation can be exploited with a high-resolution stereo imaging system. This could be of particular interest for geological investigation and mission planning, to extract detailed depth information obtained by such stereo systems, and carry out qualitative assessment of various properties of the lunar regolith such as:

1. *Micro-roughness*: One of the key properties that can be derived from high-resolution depth data is micro-roughness, which reveals the fine-scale texture of the regolith surface. In essence, surface roughness captures the variations in topography over a given horizontal distance, or baseline, and is closely tied to geomorphological processes [3]. Previous studies have measured lunar surface roughness at scales ranging from kilometres down to meters, and these investigations have shown that roughness characteristics are highly scale-dependent, with different behaviours and distributions appearing at different scales. Accurately measuring surface roughness at the millimetre level could provide valuable insights into how the lunar surface interacts with environmental factors such as micrometeorite impacts, solar wind exposure, and variations in grain size and cohesive strength [71]. For example, detailed measurements at this scale could improve our understanding of how the regolith responds to impact events and weathering processes, which is critical for both scientific research and practical applications like lander design and in-situ resource utilization. Recent work at the Chang'e-4 landing site, where stereo images were processed using photogrammetric and photoclinometric methods, has successfully produced digital elevation models with centimetre-scale resolution [14]. Similar analytical approaches could be extended to the high-resolution stereo images produced by the proposed imaging system, enabling even finer-scale mapping of micro-roughness. This, in turn, would enhance our ability to characterize the lunar surface in detail, supporting more informed geological investigations and mission planning.

2. *Grain angularity*: Another significant aspect is grain angularity, a parameter that describes the sharpness or roundness of regolith particles. Reconstructing 3D shapes of these particles is an effective way to assess their mechanical properties [72]. Evaluating grain angularity reveals critical information about the history of surface processes, including mechanical abrasion, impact fragmentation, and erosional dynamics [73]. Moreover, the 3D shape of a particle provides important insights into the overall mechanical behaviour of the regolith. Particle shapes significantly influence the regolith's mechanical strength, the angle of repose, and the compacting density, as well as its adherence tendency. In this context, the detailed study of the 3D shapes of lunar regolith particles, conducted using samples from the Apollo missions, has proven essential for understanding these properties [72]. Accurate characterization of grain angularity and particle shape is therefore vital for understanding regolith transport mechanisms and for evaluating the mechanical properties of lunar soil, particularly in applications related to in-situ resource utilization (ISRU) and the design of surface mobility systems.

3. *Grain size distribution*: The grain size distribution of the regolith is a property that can be derived from depth-resolved imaging. This distribution is essential for interpreting the regolith's porosity, compaction, and bulk behaviour. Moreover, grain size plays a pivotal role in thermal and electrical conductivity, influencing the regolith's suitability for scientific instruments or engineering applications. Two-dimensional texture and three-dimensional structure of the regolith particles captured with the high spatial resolution stereo imager, can reveal granular features and size distribution across region of interest. Computing detailed characterisation of fine-scale surface roughness and particle size distribution is demonstrated, at the Chang'e-4 landing site using Digital Terrain Model from rover collected stereo images [71]. Furthermore, when the grain size data obtained from stereo imaging is combined with heat conductivity models and thermal inertia measurements, it becomes possible to derive precise estimates of the regolith's grain size. This approach is supported by the study of Gundlach and Blum [74] in 2013, which showed how thermal inertia measurements can be effectively used to infer grain size characteristics.

4. *Surface albedo*: Topographic information can be retrieved using reflectance models through the technique of photometric stereo, a method first introduced by Heipke [75] in 1993. This approach not only allows for detailed mapping of surface geometries but also aids in the assessment of surface albedo. Surface albedo, defined as the regolith's reflectivity, is closely linked to the mineral composition and grain properties of the lunar surface. Variations in albedo often signal changes in regolith maturity and may reveal unique surface features, such as impact melts, which are critical for understanding the Moon's geological history and current state. For instance, in the context of albedo mapping, photometric parameters derived from stereo imaging can help evaluate the intrinsic reflectance properties of the surface from additional factors like topographic shading and viewing geometry. This approach has been demonstrated in Nefian's [76] work on photometric lunar surface reconstruction, where ground truth measurements facilitated the creation of large-scale albedo maps at resolutions as fine as 10 meters per pixel [3].

   Recent advancements in photoclinometric surface reconstruction techniques for

lunar applications have introduced methods such as Shape-and-Albedo-from-Shading (SAfS) to retrieve topographic information, as demonstrated in Chung Liu's study [51]. While SAfS is highly efficient for reconstructing small-scale surface features even in low textured regions, its accuracy tends to diminish when applied to larger scales. To overcome this limitation, a combined approach that integrates stereo photogrammetry with SAfS processing could be implemented.

This hybrid technique leverages the strengths of both methods, using stereo photogrammetry to capture larger-scale topographic variations and SAfS to refine small-scale details, resulting in robust surface reconstruction even in conditions of low illumination and where surface texture is limited as demonstrated by photogrammetric and photometric method of stereo image processing with Yutu-2 rover images [53]. Additional benefits arise from utilizing multiple images captured from different viewing geometries and under varying directional illuminations. This extra information further enhances and achieve more reliable reconstruction by helping to resolve ambiguities in shading and improving the overall photometric correction [3].

5. Maturity: Regolith maturation refers to the process by which freshly formed lunar soil is progressively modified through the combined effects of micrometeoroid impacts and continuous exposure to solar and cosmic charged particles [77]. This process leads to several notable changes in both the physical and chemical properties of the regolith. For instance, the mean particle size tends to decrease as continual impacts break down the grains, creating finer fragments. At the same time, the regolith becomes enriched with elements originating from the solar wind, such as hydrogen, helium, carbon, and nitrogen [78]. Additional aspect of regolith maturation is the frequent bombardment by micrometeoroids increases the concentration of specific elements associated with these impacts [79]. Another important change during maturation is the enhanced formation of a nano phase iron (np-Fe) metal layer on the surface of regolith particles, significantly altering its optical properties [80]. This feature, along with the development of agglutinate particles, small fragments that have fused together during impact events, plays a critical role in altering the mechanical and chemical behaviour of the lunar soil. As these processes progress, the overall reflectivity of the regolith decreases, leading to a lower surface albedo [81]. Concurrent with the darkening of the surface, the spectral properties of the regolith change, typically exhibiting a reddening effect that serves as an indicator of the extent of space weathering and regolith maturity.

   Together, these modifications detected with high resolution depth information, could not only provide valuable insights into the space weathering process but also enhance our understanding of lunar regolith's evolving physical and optical properties [3].

In summary, high-resolution depth information and advanced imaging techniques, such as monochromatic stereo imaging, open new avenues for characterizing lunar regolith properties. These capabilities provide deeper insights into micro-roughness, grain angularity, grain size distribution, surface albedo, and maturity, while also supporting practical applications in exploration and resource assessment. As lunar missions advance, these approaches will undoubtedly play an integral role in enhancing our understanding of the Moon's surface and enabling future scientific and engineering endeavours [3].

Chapter 5

Conclusion

5.1 Summary of Findings

This stereo camera design for prototyping in a experimental lab setup demonstrate high-resolution stereo imaging capabilities, and accurately generates depth data. Through a careful selection process and trade-off analysis between cost-effectiveness, compactness and imaging performance, the camera system employs a single monochrome CMOS detector along with a four-mirror adaptor optical configuration. This configuration was specifically designed to meet the predefined engineering requirements for future integration on a lunar rover mission. Tested under a simulated rover mounting breadboard setup, the stereo camera successfully acquires a stereo image pair and performs stereo matching processes based on effective computer vision algorithms. The camera was able to extract 3D information of the close range objects, where its capabilities of high resolution imaging and object recognition in a controlled environment is validated. The imaging performance and accuracy of the resulting stereo images were cross-validated through resolution tests, optical simulations and shape measurement experiments using a reference object with know dimensions.

The resulting spatial resolution of the camera was measured at 54 µm per pixel, with the stereo baseline length of 116 mm, an instantaneous field of view of 601 µrad per pixel and MTF > 0.45 at Nyquist frequency, exceeding the desired spatial resolution for the intended application. Additionally, the size, weight and power requirement for the system were well within the acceptable range, making it a viable candidate for integration into a lunar rover platform.

To further demonstrate the scientific applicability of the stereo imaging system, experiments were conducted to extract the static angle of repose of regolith simulant EAC-1A and NU-LHT-2M, as well as the relative surface albedo through a photometric stereo method. These experiments provided valuable insights into the physical and optical properties of lunar regolith analogues. Additionally, the 3D information was visualized using an anaglyph technique, offering an intuitive and effective method for depth perception and terrain interpretation [3].

5.2 Contributions to the Field

This project contributes to the planetary exploration missions and its advanced imaging system design proposal, by introducing a compact, cost-effective, and high performance stereo imager suitable for close range lunar surface analysis. The innovative use of four-mirror optical configuration and a monochrome CMOS sensor represents a novel approach to achieve high spatial resolution while maintaining low power consumption and space requirements, making it a suitable choice for smaller size lander missions applications. It contributes to an in depth understanding of lunar regolith properties and enhances the scientific analysis of its geo-mechanical behaviour. With

its versatile visualization techniques, such as the use of 3D anaglyphs, it provides a practical and user-friendly way to interpret depth data, which can be particularly useful for mission operators and scientists analysing terrain data in real time. The effective use of COTS components used for this project, demonstrates a fast, and practical prototyping approach which is essential for iterative optimisation of an imaging system design.

5.3 Future Directions

While a promising performance was demonstrated by the prototype stereo camera in a laboratory and simulated environment, further developments and refinement in several design areas remain unexplored. Additional experiments and evaluation needed towards the operational readiness of the prototype design includes:

1. *Integration with Machine Learning:* Future work focusing on developing and optimisation of the stereo processing pipeline by means of an advanced machine learning algorithms trained on existing stereo images dataset such as the Polar Optical Lunar Analogue Reconstruction (POLAR) dataset, or the POLAR Traverse Dataset provided by NASA Ames Research Center can be carried out [82, 83].

2. *Dust Mitigation Strategies:* Dust accumulation on the camera's optical components poses a key challenge for the imaging system in dusty lunar environment. Protective and self cleaning mechanisms, or active dust removal techniques must be further explored for long-term operational performance in harsh lunar environments.

3. *Environmental Robustness:* Further experiments considering a realistic operational conditions, the camera systems must be tested for extreme temperature variations, vibrational effects from a mobile rover and radiation exposure.

4. *Scalability and Adaptability:* Evaluation related to scalability of the system design to other terrestrial missions, such as for Mars or asteroids, with similar imaging and terrain analysis capabilities may be required.

5.4 Closing Remarks

In conclusion, the stereo camera prototype developed in this project represents a significant advancement in the field of planetary imaging and scientific data collection. By combining high-resolution imaging, compact design, and robust performance, the system supports both operational and scientific objectives in lunar surface exploration. The successful extraction of 3D terrain data and regolith properties demonstrates the system's potential for real-world applications in future lunar missions. As planetary exploration continues to evolve, the integration of advanced imaging technologies such as the one presented here will play a crucial role in enabling in-situ resource utilisation, scientific observations, as well as analysis and interaction with terrestrial environments. This work lays a solid foundation for further development and application of stereo imaging systems in the context of space exploration [3].

Bibliography

[1] W. Lovegrove and B. Brame, "Single-camera stereo vision for obstacle detection in mobile robots," p. 67640T, Sept. 2007.

[2] R. Jaumann, H. Hiesinger, M. Anand, I. A. Crawford, R. Wagner, F. Sohl, B. L. Jolliff, F. Scholten, M. Knapmeyer, H. Hoffmann, H. Hussmann, M. Grott, S. Hempel, U. Köhler, K. Krohn, N. Schmitz, J. Carpenter, M. Wieczorek, T. Spohn, M. S. Robinson, and J. Oberst, "Geology, geochemistry, and geophysics of the Moon: Status of current understanding," *Planetary and Space Science*, vol. 74, pp. 15–41, Dec. 2012.

[3] Microsoft, "Copilot for microsoft 365," 2025. AI-powered assistant integrated into Microsoft 365 applications.

[4] W. Wan, J. Wang, K. Di, J. Li, Z. Liu, P. Man, Y. Wang, T. Yu, C. Liu, and L. Li, "Enhanced Lunar Topographic Mapping Using Multiple Stereo Images Taken by Yutu-2 Rover with Changing Illumination Conditions," *Photogrammetric Engineering & Remote Sensing*, vol. 87, pp. 567–576, Aug. 2021.

[5] J.-F. Yang, C.-L. Li, B. Xue, P. Ruan, W. Gao, W.-D. Qiao, D. Lu, X.-L. Ma, F. Li, Y.-H. He, T. Li, X. Ren, and X.-T. Yan, "Panoramic camera on the Yutu lunar rover of the Chang'e-3 mission," *Research in Astronomy and Astrophysics*, vol. 15, p. 1867, Nov. 2015.

[6] K. Di, M. Zhu, Z. Yue, Y. Lin, W. Wan, Z. Liu, S. Gou, B. Liu, M. Peng, Y. Wang, S. Niu, J. Zhang, J. Li, J. Xie, L. Xi, J. Yang, and B. Xue, "Topographic Evolution of Von Kármán Crater Revealed by the Lunar Rover Yutu-2," *Geophysical Research Letters*, vol. 46, pp. 12764–12770, Nov. 2019.

[7] H. Lin, Y. Yang, Y. Lin, Y. Liu, Y. Wei, S. Li, S. Hu, W. Yang, W. Wan, R. Xu, Z. He, X. Liu, Y. Xing, C. Yu, and Y. Zou, "Photometric properties of lunar regolith revealed by the Yutu-2 rover," *Astronomy & Astrophysics*, vol. 638, p. A35, June 2020. Publisher: EDP Sciences.

[8] K. Di, Z. Liu, W. Wan, M. Peng, B. Liu, Y. Wang, S. Gou, and Z. Yue, "Geospatial technologies for Chang'e-3 and Chang'e-4 lunar rover missions," *Geo-spatial Information Science*, Jan. 2020.

[9] J. N. Maki, J. F. Bell III, K. E. Herkenhoff, S. W. Squyres, A. Kiely, M. Klimesh, M. Schwochert, T. Litwin, R. Willson, A. Johnson, M. Maimone, E. Baumgartner, A. Collins, M. Wadsworth, S. T. Elliot, A. Dingizian, D. Brown, E. C. Hagerott, L. Scherr, R. Deen, D. Alexander, and J. Lorre, "Mars Exploration Rover Engineering Cameras," *Journal of Geophysical Research: Planets*, vol. 108, no. E12, 2003.

[10] M. C. Malin, M. A. Ravine, M. A. Caplinger, F. Tony Ghaemi, J. A. Schaffner, J. N. Maki, J. F. Bell III, J. F. Cameron, W. E. Dietrich, K. S. Edgett, L. J.

Edwards, J. B. Garvin, B. Hallet, K. E. Herkenhoff, E. Heydari, L. C. Kah, M. T. Lemmon, M. E. Minitti, T. S. Olson, T. J. Parker, S. K. Rowland, J. Schieber, R. Sletten, R. J. Sullivan, D. Y. Sumner, R. Aileen Yingst, B. M. Duston, S. McNair, and E. H. Jensen, "The Mars Science Laboratory (MSL) Mast cameras and Descent imager: Investigation and instrument descriptions," *Earth and Space Science*, vol. 4, no. 8, pp. 506–539, 2017.

[11] J. N. Maki, D. Gruel, C. McKinney, M. A. Ravine, M. Morales, D. Lee, R. Willson, D. Copley-Woods, M. Valvo, T. Goodsall, J. McGuire, R. G. Sellar, J. A. Schaffner, M. A. Caplinger, J. M. Shamah, A. E. Johnson, H. Ansari, K. Singh, T. Litwin, R. Deen, A. Culver, N. Ruoff, D. Petrizzo, D. Kessler, C. Basset, T. Estlin, F. Alibay, A. Nelessen, and S. Algermissen, "The Mars 2020 Engineering Cameras and Microphone on the Perseverance Rover: A Next-Generation Imaging System for Mars Exploration," *Space Science Reviews*, vol. 216, p. 137, Nov. 2020.

[12] J. F. Bell, J. N. Maki, G. L. Mehall, M. A. Ravine, M. A. Caplinger, Z. J. Bailey, S. Brylow, J. A. Schaffner, K. M. Kinch, M. B. Madsen, A. Winhold, A. G. Hayes, P. Corlies, C. Tate, M. Barrington, E. Cisneros, E. Jensen, K. Paris, K. Crawford, C. Rojas, L. Mehall, J. Joseph, J. B. Proton, N. Cluff, R. G. Deen, B. Betts, E. Cloutis, A. J. Coates, A. Colaprete, K. S. Edgett, B. L. Ehlmann, S. Fagents, J. P. Grotzinger, C. Hardgrove, K. E. Herkenhoff, B. Horgan, R. Jaumann, J. R. Johnson, M. Lemmon, G. Paar, M. Caballo-Perucha, S. Gupta, C. Traxler, F. Preusker, M. S. Rice, M. S. Robinson, N. Schmitz, R. Sullivan, and M. J. Wolff, "The Mars 2020 Perseverance Rover Mast Camera Zoom (Mastcam-Z) Multispectral, Stereoscopic Imaging Investigation," *Space Science Reviews*, vol. 217, p. 24, Feb. 2021.

[13] A. Coates, R. Jaumann, A. Griffiths, C. Leff, N. Schmitz, J.-L. Josset, G. Paar, M. Gunn, E. Hauber, C. Cousins, R. Cross, P. Grindrod, J. Bridges, M. Balme, S. Gupta, I. Crawford, P. Irwin, R. Stabbins, D. Tirsch, J. Vago, T. Theodorou, M. Caballo-Perucha, and G. Osinski, "The PanCam Instrument for the ExoMars Rover," *Astrobiology*, vol. 17, pp. 511–541, July 2017.

[14] B. Wu, Y. Li, W. C. Liu, Y. Wang, F. Li, Y. Zhao, and H. Zhang, "Centimeter-resolution topographic modeling and fine-scale analysis of craters and rocks at the Chang'E-4 landing site," *Earth and Planetary Science Letters*, vol. 553, p. 116666, Jan. 2021.

[15] Y.-J. Zhang, *Handbook of Image Engineering*. Singapore: Springer, 2021.

[16] R. Hartley and A. Zisserman, *Multiple View Geometry in Computer Vision*. Cambridge University Press, 2 ed., Mar. 2004.

[17] A. Goshtasby and W. A. Gruver, "Design of a single-lens stereo camera system," *Pattern Recognition*, vol. 26, pp. 923–937, June 1993.

[18] Y. Nishimoto and Y. Shirai, "A feature-based stereo model using disparity histograms of multi-resolution channels," *Advanced Robotics*, vol. 3, pp. 17–33, Jan. 1988.

[19] W. Teoh and X. Zhang, "An inexpensive stereoscopic vision system for robots," in *Proceedings. 1984 IEEE International Conference on Robotics and Automation*, vol. 1, (Atlanta, GA, USA), pp. 186–189, Institute of Electrical and Electronics Engineers, 1984.

[20] S. Nene and S. Nayar, "Stereo with mirrors," in *Sixth International Conference on Computer Vision (IEEE Cat. No.98CH36271)*, pp. 1087–1094, Jan. 1998.

[21] D. Lee and I. Kweon, "A novel stereo camera system by a biprism," *IEEE Transactions on Robotics and Automation*, vol. 16, pp. 528–541, Oct. 2000. Conference Name: IEEE Transactions on Robotics and Automation.

[22] H. Luo, L. Yu, and B. Pan, "Design and validation of a demand-oriented single-camera stereo-DIC system with a four-mirror adapter," *Measurement*, vol. 186, p. 110083, Dec. 2021.

[23] M. Pankow, B. Justusson, and A. M. Waas, "Three-dimensional digital image correlation technique using single high-speed camera for measuring large out-of-plane displacements at high framing rates," *Applied Optics*, vol. 49, p. 3418, June 2010. ADS Bibcode: 2010ApOpt..49.3418P.

[24] G. Besnard, J.-M. Lagrange, F. Hild, S. Roux, and C. Voltz, "Characterization of Necking Phenomena in High-Speed Experiments by Using a Single Camera," *EURASIP Journal on Image and Video Processing*, vol. 2010, pp. 1–15, Dec. 2010.

[25] A. Greenleaf, *Photographic Optics*. No. S. 5 in Photographic Optics, Macmillan, 1950.

[26] "Ansys® zemax OpticStudio Premium," 2023.

[27] R. Chipman and W. Lam, "The point spread function in paraxial optics," in *Current Developments in Lens Design and Optical Engineering XVI* (V. Mahajan, S. Thibault, V. Mahajan, S. Thibault, R. Johnson, and R. Johnson, eds.), Proceedings of SPIE - The International Society for Optical Engineering, SPIE, 2015.

[28] W. J. Smith, "Chapter 15.8 the modulation transfer function," in *Modern Optical Engineering*, pp. 385–390, McGraw-Hill Education, 4th ed., 2008.

[29] V. S. Engelschiøn, S. R. Eriksson, A. Cowley, M. Fateri, A. Meurisse, U. Kueppers, and M. Sperl, "EAC-1A: A novel large-volume lunar regolith simulant," *Scientific Reports*, vol. 10, p. 5473, Mar. 2020.

[30] "ThorCam™ Software for Scientific and Compact USB Cameras," 2022.

[31] G. Bradski, "The OpenCV Library," *Dr. Dobb's Journal of Software Tools*, 2000.

[32] S. Maamir and A. K. Haghi, eds., *Mechanical and physico-chemical characteristics of modified materials: performance evaluation and selection*. Oakville, ON Waretown, NJ: Apple Academic Press, 2016.

[33] J.-Y. Bouguet, "Camera Calibration Toolbox for Matlab," May 2022.

[34] Z. Zhang, "A flexible new technique for camera calibration," *IEEE Transactions on Pattern Analysis and Machine Intelligence*, vol. 22, pp. 1330–1334, Nov. 2000.

[35] F. Cao, R. Wang, and L. Zhang, "Feature extraction and stereo matching algorithm for lunar surface," in *Proceedings 2011 International Conference on Transportation, Mechanical, and Electrical Engineering (TMEE)*, pp. 1399–1402, Dec. 2011.

[36] L. Zhang, A. Cao, and Y. Du, "Study on Image Feature Point Extraction Algorithm and Stereo Matching Technique," *Journal of Computational and Theoretical Nanoscience*, vol. 13, pp. 2938–2944, May 2016.

[37] D. Lowe, "Object recognition from local scale-invariant features," in *Proceedings of the Seventh IEEE International Conference on Computer Vision*, vol. 2, pp. 1150–1157 vol.2, Sept. 1999.

[38] X.-f. Feng and B. Fang, "Algorithm for epipolar geometry and correcting monocular stereo vision based on a plane mirror," *Optik*, vol. 226, p. 165890, Jan. 2021.

[39] H. Hirschmuller, "Stereo Processing by Semiglobal Matching and Mutual Information," *IEEE Transactions on Pattern Analysis and Machine Intelligence*, vol. 30, pp. 328–341, Feb. 2008.

[40] F. Matsuura and N. Fujisawa, "Anaglyph stereo visualization by the use of a single image and depth information," *Journal of Visualization*, vol. 11, pp. 79–86, Mar. 2008.

[41] W. Alkhadour, S. Ipson, J. Zraqou, R. Qahwaji, and J. Haigh, "Creating a Color Anaglyph from a Pseudo-Stereo Pair of Images," in *Image and Signal Processing*, June 2009.

[42] M. W. Powell, J. S. Norris, M. A. I. Vona, P. G. Backes, and J. V. Wick, "Scientific visualization for the Mars Exploration Rovers," 2005.

[43] T. M. Inc., "Matlab computer vision toolbox version: 24.2 (r2024b)," 2024.

[44] C. I. Calle and C. R. Buhler, "Measurement of the Angle of Repose of Apollo 14 Lunar Sample 14163," vol. 2141, p. 5030, Feb. 2020. ADS Bibcode: 2020LPICo2141.5030C.

[45] H. M. Beakawi Al-Hashemi and O. S. Baghabra Al-Amoudi, "A review on the angle of repose of granular materials," *Powder Technology*, vol. 330, pp. 397–417, May 2018.

[46] P. Easter, J. Long-Fox, D. Britt, and J. Brisset, "The effect of particle size distribution on lunar regolith simulant angle of repose," *Advances in Space Research*, vol. 74, pp. 3437–3447, Oct. 2024.

[47] F. Elekes and E. J. R. Parteli, "An expression for the angle of repose of dry cohesive granular materials on Earth and in planetary environments," *Proceedings of the National Academy of Sciences of the United States of America*, vol. 118, p. e2107965118, Sept. 2021.

[48] J.-C. Ginés-Palomares, M. Fateri, T. Schubert, L. de Peindray d'Ambelle, S. Simon, G. J. G. Gluth, J. Günster, and A. Zocca, "Material aspects of sintering of EAC-1A lunar regolith simulant," *Scientific Reports*, vol. 13, p. 23053, Dec. 2023.

[49] D. Stoeser, D. Rickman, and S. Wilson, "Design and Specifications for the Highland Regolith Prototype Simulants NU-LHT-1M and -2M," Tech. Rep. NASA/TM-2010-216438, Aug. 2011. NTRS Author Affiliations: Geological Survey, NASA Marshall Space Flight Center NTRS Document ID: 20110008071 NTRS Research Center: Marshall Space Flight Center (MSFC).

[50] G. Zanotti, I. Troisi, A. Dottori, and M. R. Lavagna, "Planetary Soil Simulant Characterisation: NU-LHT-2M Study Case to Support Oxygen Extraction Lab Tests with a Low-Temperature Carbothermal Process," *Aerospace*, vol. 11, p. 295, Apr. 2024.

[51] W. Chung Liu, B. Wu, and C. Wöhler, "Effects of illumination differences on photometric stereo shape-and-albedo-from-shading for precision lunar surface reconstruction," *ISPRS Journal of Photogrammetry and Remote Sensing*, vol. 136, pp. 58–72, Feb. 2018.

[52] B. K. P. Horn, R. J. Woodham, and M. Silverwilliam, "Determining Shape and Reflectance Using Multiple Images," Aug. 1978.

[53] M. Peng, K. Di, Y. Wang, W. Wan, Z. Liu, J. Wang, and L. Li, "A Photogrammetric-Photometric Stereo Method for High-Resolution Lunar Topographic Mapping Using Yutu-2 Rover Images," *Remote Sensing*, vol. 13, p. 2975, July 2021.

[54] R. J. Woodham, "Photometric Method For Determining Surface Orientation From Multiple Images," *Optical Engineering*, vol. 19, Feb. 1980.

[55] P. F. Luo and J. N. Chen, "Measurement of curved-surface deformation in cylindrical coordinates," *Experimental Mechanics*, vol. 40, pp. 345–350, Dec. 2000.

[56] S. P. Campbell, "Use of a Nyquist chart for camera system evaluation," in *Sensors and Camera Systems for Scientific, Industrial, and Digital Photography Applications* (N. Sampat, T. Yeh, M. M. Blouke, N. Sampat, G. M. W. Jr., and T. Yeh, eds.), vol. 3965, pp. 230 – 234, International Society for Optics and Photonics, SPIE, 2000.

[57] A. G. Hayes, P. Corlies, C. Tate, M. Barrington, J. F. Bell, J. N. Maki, M. Caplinger, M. Ravine, K. M. Kinch, K. Herkenhoff, B. Horgan, J. Johnson, M. Lemmon, G. Paar, M. S. Rice, E. Jensen, T. M. Kubacki, E. Cloutis, R. Deen, B. L. Ehlmann, E. Lakdawalla, R. Sullivan, A. Winhold, A. Parkinson, Z. Bailey, J. Van Beek, P. Caballo-Perucha, E. Cisneros, D. Dixon, C. Donaldson, O. B. Jensen, J. Kuik, K. Lapo, A. Magee, M. Merusi, J. Mollerup, N. Scudder, C. Seeger, E. Stanish, M. Starr, M. Thompson, N. Turenne, and K. Winchell, "Pre-Flight Calibration of the Mars 2020 Rover Mastcam Zoom (Mastcam-Z) Multispectral, Stereoscopic Imager," *Space Science Reviews*, vol. 217, p. 29, Mar. 2021.

[58] F. Van Den Bergh, "Deferred slanted-edge analysis: a unified approach to spatial frequency response measurement on distorted images and color filter array subsets," *Journal of the Optical Society of America A*, vol. 35, p. 442, Mar. 2018.

[59] "MTF mapper," Nov. 2024.

[60] A. Kiran Kumar and A. Roy Chowdhury, "Hyper-spectral imager in visible and near-infrared band for lunar compositional mapping," *Journal of earth system science*, vol. 114, pp. 721–724, 2005.

[61] A. Lahiri, "Chapter 3 - ray optics: Optical systems and optical imaging," in *Basic Optics* (A. Lahiri, ed.), pp. 203–307, Amsterdam: Elsevier, 2016.

[62] T. J. Stubbs, R. R. Vondrak, and W. M. Farrell, "Impact of dust on lunar exploration," *Dust in planetary systems*, vol. 643, pp. 239–243, 2007.

[63] M. Horányi, J. R. Szalay, and X. Wang, "The lunar dust environment: concerns for Moon-based astronomy," *Philosophical Transactions of the Royal Society A: Mathematical, Physical and Engineering Sciences*, vol. 382, p. 20230075, Mar. 2024. Publisher: Royal Society.

[64] B. Hapke, "Bidirectional reflectance spectroscopy: 1. theory," *Journal of Geophysical Research: Solid Earth*, vol. 86, no. B4, pp. 3039–3054, 1981.

[65] Y. Shkuratov, L. Starukhina, H. Hoffmann, and G. Arnold, "A model of spectral albedo of particulate surfaces: Implications for optical properties of the moon," *Icarus*, vol. 137, no. 2, pp. 235–246, 1999.

[66] S. Li and L. Li, "Radiative transfer modeling for quantifying lunar surface minerals, particle size, and submicroscopic metallic fe," *Journal of Geophysical Research: Planets*, vol. 116, no. E9, 2011.

[67] R. Jaumann, N. Schmitz, A. Koncz, H. Michaelis, S. E. Schroeder, S. Mottola, F. Trauthan, H. Hoffmann, T. Roatsch, D. Jobs, J. Kachlicki, B. Pforte, R. Terzer, M. Tschentscher, S. Weisse, U. Mueller, L. Perez-Prieto, B. Broll, A. Kruselburger, T.-M. Ho, J. Biele, S. Ulamec, C. Krause, M. Grott, J.-P. Bibring, S. Watanabe, S. Sugita, T. Okada, M. Yoshikawa, and H. Yabuta, "The Camera of the MASCOT Asteroid Lander on Board Hayabusa 2," *Space Science Reviews*, vol. 208, pp. 375–400, July 2017.

[68] J. Connolly and W. D. Carrier, "An Engineering Guide to Lunar Geotechnical Properties," in *2023 IEEE Aerospace Conference*, pp. 1–9, Mar. 2023. ISSN: 1095-323X.

[69] E. N. Slyuta, E. A. Grishakina, V. Y. Makovchuk, and I. A. Agapkin, "Lunar soil-analogue VI-75 for large-scale experiments," *Acta Astronautica*, vol. 187, pp. 447–457, Oct. 2021.

[70] L. Ding, Z. Deng, H. Gao, K. Nagatani, and K. Yoshida, "Planetary rovers' wheel–soil interaction mechanics: new challenges and applications for wheeled mobile robots," *Intelligent Service Robotics*, vol. 4, pp. 17–38, Jan. 2011.

[71] D. Guo, W. Fa, B. Wu, Y. Li, and Y. Liu, "Millimeter- to Decimeter-Scale Surface Roughness of the Moon at the Chang'e-4 Exploration Region," *Geophysical Research Letters*, vol. 48, no. 19, p. e2021GL094931, 2021.

[72] J. Katagiri, T. Matsushima, Y. Yamada, A. Tsuchiyama, T. Nakano, K. Uesugi, M. Ohtake, and K. Saiki, "Investigation of 3D Grain Shape Characteristics of Lunar Soil Retrieved in Apollo 16 Using Image-Based Discrete-Element Modeling," *Journal of Aerospace Engineering*, vol. 28, p. 04014092, July 2015.

[73] A. Tsuchiyama, T. Sakurama, T. Nakano, K. Uesugi, M. Ohtake, T. Matsushima, K. Terakado, and E. M. Galimov, "Three-dimensional shape distribution of lunar regolith particles collected by the Apollo and Luna programs," *Earth, Planets and Space*, vol. 74, p. 172, Nov. 2022.

[74] B. Gundlach and J. Blum, "A new method to determine the grain size of planetary regolith," *Icarus*, vol. 223, pp. 479–492, Mar. 2013.

[75] C. Heipke, "Integration of digital image matching and multi image shape from shading," *International archives of photogrammetry and remote sensing*, vol. 29, pp. 832–832, 1993.

[76] A. V. Nefian, O. Alexandrov, Z. Moratto, T. Kim, and R. A. Beyer, "Photometric Lunar surface reconstruction," in *2013 IEEE International Conference on Image Processing*, pp. 2354–2357, Sept. 2013. ISSN: 2381-8549.

[77] R. V. Morris, "The surface exposure (maturity) of lunar soils: Some concepts and Is/FeO compilation.," *Lunar and Planetary Science Conference Proceedings*, vol. 2, pp. 2287–2297, Jan. 1978.

[78] R. M. Housley, "Solar Wind and Micrometeorite Effects in the Lunar Regolith," *Philosophical Transactions of the Royal Society of London. Series A, Mathematical and Physical Sciences*, vol. 285, no. 1327, pp. 363–367, 1977.

[79] E. G. Sorokin, O. I. Yakovlev, E. N. Slyuta, M. V. Gerasimov, M. A. Zaitsev, V. D. Shcherbakov, K. M. Ryazantsev, and S. P. Krasheninnikov, "Experimental Modeling of a Micrometeorite Impact on the Moon," *Geochemistry International*, vol. 58, pp. 113–127, Feb. 2020.

[80] M. Xiong, Y. Wu, W. Yao, Z. Chen, Y. Yu, X. Li, P. Yan, X. Li, and X. Zeng, "The Formation Mechanisms of np-Fe in Lunar Regolith: A Review," *Materials*, vol. 17, p. 5866, Jan. 2024.

[81] J. B. Adams and M. P. Charette, "Effects of maturation on the reflectance of the lunar regolith: Apollo 16 — A case study," *The moon*, vol. 13, pp. 293–299, Mar. 1975.

[82] U. Wong, A. Nefian, L. Edwards, X. Buoyssounouse, P. M. Furlong, M. Deans, and T. Fong, "Polar optical lunar analog reconstruction (polar) stereo dataset," 2017.

[83] M. Hansen, U. Wong, and T. Fong, "The POLAR Traverse Dataset: A Dataset of Stereo Camera Images Simulating Traverses across Lunar Polar Terrain under Extreme Lighting Conditions," Mar. 2024. arXiv:2403.12194 [cs].